

Quantum Parity Detectors: a qubit based particle detection scheme with meV thresholds for rare-event searches

K. Ramanathan,^{1,2,*} J. E. Parker,¹ L. M. Joshi,³ A. D. Beyer,⁴
P. M. Echternach,⁴ S. Rosenblum,³ B. J. Sandoval,¹ and S R. Golwala¹

¹Department of Physics, California Institute of Technology, Pasadena, CA, 91125, USA

²Department of Physics, Washington University in St. Louis, St. Louis, MO, 63130, USA

³Department of Condensed Matter Physics, Weizmann Institute of Science, Rehovot, Israel

⁴Jet Propulsion Laboratory, California Institute of Technology, Pasadena, CA 91109, USA

(Dated: May 28, 2024)

The next generation of rare-event searches, such as those aimed at determining the nature of particle dark matter or in measuring fundamental neutrino properties, will benefit from particle detectors with thresholds at the meV scale, 100–1000× lower than currently available. Quantum parity detectors (QPDs) are a novel class of proposed quantum devices that use the tremendous sensitivity of superconducting qubits to quasiparticle tunneling events as their detection concept. As envisioned, phonons generated by particle interactions within a crystalline substrate cause an eventual quasiparticle cascade within a surface patterned superconducting qubit element. This process alters the fundamental charge parity of the device in a binary manner, which can be used to deduce the initial properties of the energy deposition. We lay out the operating mechanism, noise sources, and expected sensitivity of QPDs based on a spectrum of charge-qubit types and readout mechanisms and detail an R&D pathway to demonstrating sensitivity to sub-eV energy deposits.

I. INTRODUCTION

A key science requirement for the next generation of rare-event searches, such as those looking for very light particle dark matter or expanding neutrino measurement regimes [1, 2], is the ability to identify energy deposits \ll eV within a macroscopic ($O(\text{gm})$) target mass. For example, theoretically well-motivated particle dark matter candidates with $O(10\text{--}10^4)$ keV c^{-2} masses may interact with an atomic target and kinematically transfer only $O(1\text{--}10^3)$ meV [3]. Further complicating this picture is that, as the interaction energy (momentum) scale drops below the \sim eV (\sim keV c^{-1}) level in common crystalline target materials, it is predominantly only collective excitations that are created, the most common of which are phonons (lattice vibration quanta) [4]. Transition Edge Sensors (TESs) [5] have demonstrated the lowest thresholds for detection of phonons, at the $O(\text{eV})$ level [6], and Kinetic Inductance Detectors (KIDs) are on a similarly trajectory [7, 8]. However, it remains an outstanding particle physics community priority to demonstrate *single-phonon-sensitive detectors* as tools in the search for new physics [3].

Concurrently, the past decades have seen rapid progress in the field of superconducting qubits for Quantum Information Science (QIS) [9]. These computing building blocks have been shown to be affected by environmental radioactivity, producing correlated errors across an entire wafer [10], induced by charge and phonons produced within the substrate. An active area of QIS R&D is in mitigating these effects by engineering phonon or quasiparticle absorbers and sinks [11].

Crucially, the relevant energy scales of the physical phenomena affecting qubit coherence is matched to the particle physics requirements discussed above. For example, in a common qubit material like aluminum with a superconducting Cooper

pair-breaking gap of $2\Delta \approx 400 \mu\text{eV}$, any resultant *quasiparticle* (broken Cooper-pair electron) from phonon absorption can tunnel across the Josephson Junction at the heart of the circuit. This tunneling process has a fingerprint, modifying the energy level structure of the qubit and possibly decohering it [12–14].

Quantum Capacitance Detectors (QCDs) [15, 16], based on Single Cooper-Pair Box (CPB) qubit designs [9], exploit this quasiparticle tunneling process for far-IR radiation detection, and they have since demonstrated the ability to count single 1.5 THz photons [17] using an RF-based readout scheme that lends itself to easy multiplexing, with over 400 QCDs chained on a single feedline [18]. It is natural to consider whether such sensors can be repurposed as generic phonon-mediated detectors for rare-event searches.

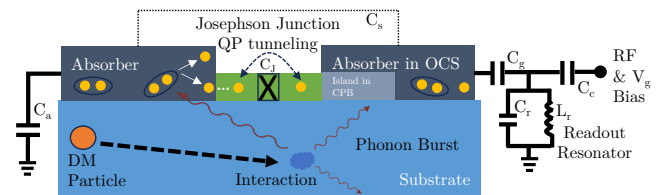


FIG. 1: Schematic of the operating principle of both QPD styles. A Josephson Junction (green) is sandwiched either by large superconducting absorbers (OCS, gray) or an absorber and small island (CPB, light gray). The structure is embedded in a resonant readout circuit, with identified circuit terms, and patterned on the surface of a crystalline substrate (blue).

This note lays out the operating principles of exactly such a novel class of pair-breaking detector we term Quantum Parity Detectors (QPDs)¹. We also extend the underlying physics

¹ We became aware of similar concepts, like the SQUAT [19] and [20] while designing and fabricating our QPDs over the past year.

* karthikr@caltech.edu

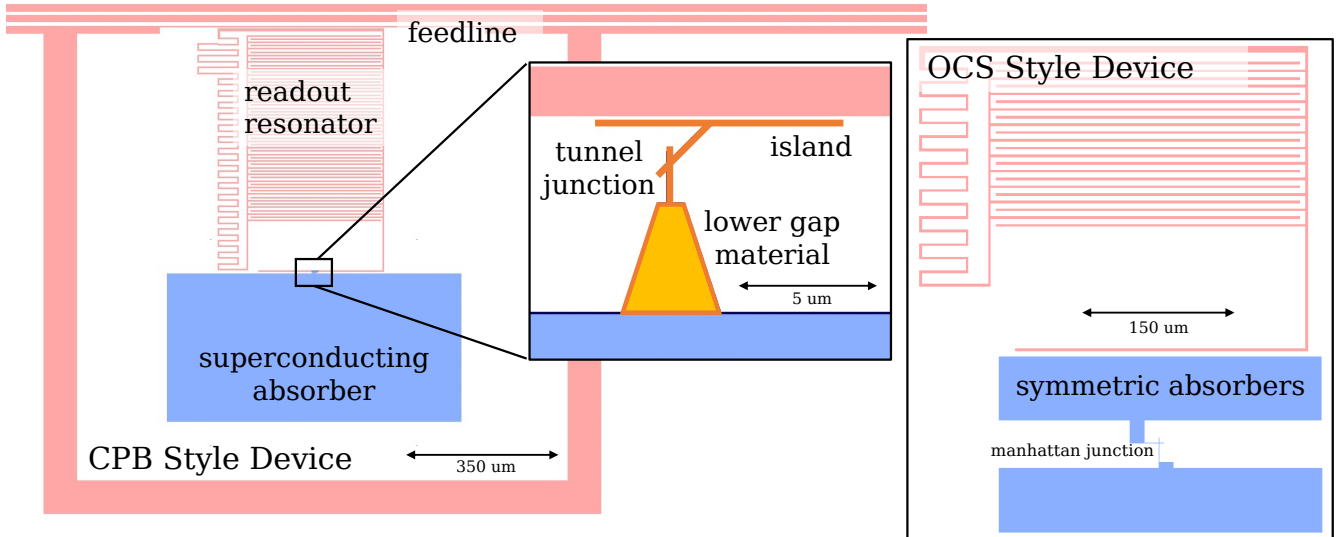


FIG. 2: Mask layouts of QPD devices. *Left and Inset*: QCD derived sensor, with large absorber connected to small island. We note that the the island region can be fabricated from a lower gap material to the absorber, engendering quasiparticle trapping and multiplication. *Right*: OCS transmon, with mostly identical components except larger, symmetric pads that introduce a shunt capacitance. A similar statement about trapping applies in this geometry as well.

of QCDs to a different qubit architecture — Offset Charge Sensitive (OCS) transmons [21, 22]. Sec. II will outline the detector concept, Sec. III will describe relevant physical principles along with the readout mechanism, Sec. IV will detail the estimated performance along with cataloging expected noise sources, and finally Sec. IV D will outline future choices and challenges to be addressed.

II. DEVICE CONCEPT

A schematic overview of the device concept is given in Fig. 1. A rare-event interaction such as that of a dark matter particle scattering within the substrate creates an energy deposit E_{dep} that will result in the production and propagation of phonons. The substrate is a high-resistivity, macroscopically thick crystal, typically $O(\text{gm})$ in mass, with silicon or sapphire (Al_2O_3) being common choices for rare-event experiment architectures [23, 24]. The QPD portion consists of two superconducting pads patterned on the substrate surface coupled by a $O(100)$ nm Josephson Junction [25], akin to a traditional qubit design [22, 26]. Depending on whether it is a OCS or QCD-style sensor, with heritage from transmon or CPB qubits respectively, the pads can be symmetrically large (*absorber-absorber*) or asymmetric (*absorber-island*). The produced phonons impinge on and can be absorbed by the pads, breaking Cooper-pairs and creating quasiparticles. This modulation of quasiparticle density, δn_{qp} , is the quantity of interest sensed by the QPD via the coupled readout resonator (either thin-film or cavity geometry) of bare frequency $\omega_r (= 1/\sqrt{L_r C_r} = 2\pi f_r)$. The absorbers and junctions are thin-film, with $O(10)$ nm thick aluminum and hafnium (due to its lower pair-breaking energy) investigated here as plausible

candidates. Aluminum is the standard material for fabrication of QIS circuits and junctions, while hafnium tunnel junctions have been demonstrated in the literature [27, 28]. Proposed layouts of the two types of QPDs can be seen in Fig. 2, highlighting the discussed elements of the absorber, island, resonator, readout feedline, and Josephson Junction.

It should be pointed out that the quasiparticles produced in the absorber can be *trapped* and *multiplied* in a lower gap material [29, 30] (of which the junction is made of as well) with benefits briefly discussed in Sec. IV for an Al absorber plus Hf trap-junction setup. In such a scheme, quasiparticles in the absorber that impinge on the overlap region with the trap material experience a lower gap there, where they may become trapped, potentially creating new quasiparticles in the process. However, the majority of this paper will be spent on discussing devices composed of single materials in order to elucidate basic operating principles while eliding the complicated modeling of quasiparticle transport physics [31, 32].

Charge qubits (which includes CPBs and transmons) are superconducting circuits engineered to have addressable “charge” basis states — simplistically, their properties are determined by the number of Cooper pairs present on an isolated island [9, 22, 33]. As will be elucidated in Sec. III B, charge qubits can be treated as anharmonic quantum oscillators, reducible to a two-level quantum system, and thus have found great use as building blocks for quantum computing [34, 35]. However, due to their environmental sensitivity, these schemes can be affected by the incoherent tunneling of quasiparticles across the Josephson Junction. The ground state of the qubit is actually a sinusoidal function of the offset charge, n_g , on the island, as shown in Fig. 3 Top. The addition of a single charge can be interpreted as a change in n_g by 0.5, causing the qubit to switch between the “odd” and “even” curves, with a difference

in energy of δE . Hence, it is said that addition or removal of a charge changes the “parity” of the system [21]. Even in the case of very low temperature operation, with a thermally suppressed quasiparticle population, non-equilibrium quasiparticles from other sources pose this risk of quasiparticle poisoning [36], potentially ruining quantum coherence. Regardless of QPD type, a microwave resonator with bare resonant frequency ω_r can be capacitively coupled to the qubit to monitor the qubit parity². Any excess population of non-equilibrium quasiparticles created by phonon absorption can tunnel across the junction and thus be sensed by each tunneling event’s impact on ω_r , with the tunneling rate ($O(1)$ kHz $\cdot\mu\text{m}^3$) proportional to this quasiparticle density. The excess rate of parity transitions should thus be proportional to the original substrate energy deposition, providing a basis for using QPDs for particle detection [17]. Fig. 3 Bottom shows an example of the expected resonator response to parity shifts, called a telegraph signal. We consider even parity to be zero or an even number of quasiparticles (with odd being the complement) to have tunneled across the barrier. Additionally, an applied voltage bias V_g , adjusted with the aid of a gate capacitor C_g , allows for tuning of the gate charge operating point to maximize the observed parity switch signal.

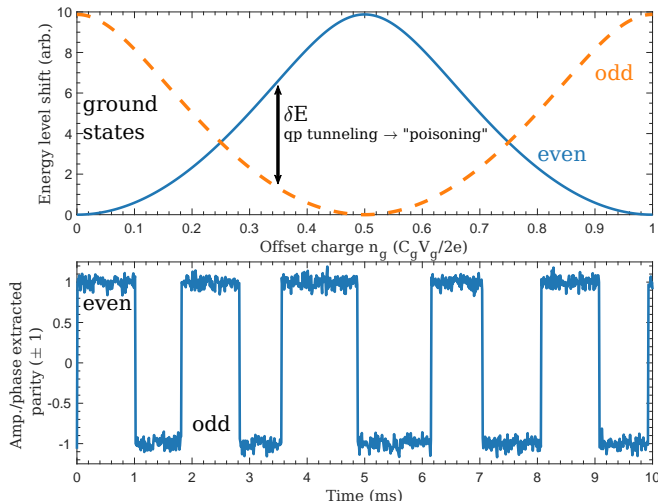


FIG. 3: *Top*: Stylized ground-state energy level shifts for a charge qubit, showing the different curves for even and odd number of charges on the island, with δE difference in energy. A quasiparticle tunneling event shifts the qubit from one state to the other. *Bottom*: Expected extracted resonator telegraph signal. Each tunneling event causes a parity shift and thus an amplitude/phase change in the resonator signal, and this rate is proportional to the quasiparticle density within the absorbers.

In the QPD scheme, the underlying qubits are always operated in their ground state, requiring no complex state manipulation. Additionally, the sensors do not interact with each

other. Thus, QPDs have the added benefit of easy multiplexability, as each qubit can be coupled to a readout resonator of a slightly different resonant frequency. The expected maximal dispersive shift of a GHz resonator due to a parity switching event will be between 100 kHz to 10 MHz, depending on the QPD style. Furthermore, even the lower bound shift is a significant fraction of the resonators FWHM f_r/Q for a loaded quality factor $Q_r \sim 10^4$ — easily resolvable given the expected $O(100)$ Hz nominal resonator frequency readout noise [37, 38]. In other words, any reasonable RF probe will be able to continuously distinguish even vs. odd states. There is however the added complexity of having to tune the gate charges for each QPD, due to differences between QPDs arising from charge inhomogeneities and associated drifts. For a single QPD this problem can be overcome by actively monitoring n_g via the size of observed parity shifts (or other related variables, such as changes in the qubit transition frequency) and adjusting the voltage gate bias, a technique already used in qubit systems [39]. For multiplexed systems, we surmount this problem, at least in the OCS scheme, using an alternate technique of sweeping the gate bias through one full period of gate charge at a sufficiently high frequency, faster than the expected tunneling rate for small energy deposits [17]. The output signal in this case is periodic and a tunneling event parity shift causes a discrete phase shift in this pattern.

III. DEVICE PHYSICS

A. Phonon & Quasiparticle Response

Following the description in Ref. [40], the initial burst of phonons will be around the Debye frequency of $O(10)$ THz. Decay and scattering processes cause these relatively high-frequency phonons to downconvert within a few μm to phonons that propagate quasi-diffusively with a speed less than the crystal’s sound speed. Once the phonon energies are low enough (still meV and thus athermal for a sub-Kelvin substrate), the mean free path exceeds the crystal dimensions. They thus travel ballistically at the sound speed and are subject primarily to reflections at the bare crystal surfaces or absorption at interfaces between the crystal and other materials (thin films and mounting points). Typical optical branch phonon energies in commonly considered crystalline substrates are of $O(10)$ meV with the high tail of acoustic phonons ($k_B T_{\text{debye}}$) at this level.

The absorption of phonons into a superconducting film on the surface engenders a pulse-like time-varying change in the quasiparticle density $\delta n_{\text{qp}}(t)$. Nominally, there are multiple time-scales that need to be considered for both phonons and quasiparticles, including cyclic transfer of energy between both channels [41]. In tandem, there are a string of efficiencies modulating the transfer of energy between each step of the overall process, for example factoring in phonon losses to surface-mediated down-conversion. Various references have cataloged said efficiencies and time-scales [32, 42] but crucially there is no singular literature model that reproduces observed pulse shapes across various detector modalities. Rather

² In the CPB case, the parity shift is interpreted as a change in the device capacitance (hence Quantum Capacitance Detector)

it seems experiment-specific factors of material selection, geometry, mounting, film properties, application of a bias field, etc. all impact the detector response and must be disentangled empirically. As such, we limit ourselves to a simplified model for δn_{qp} , useful to get a flavor of detector operation, and only briefly discuss details of effective phonon energy collection.

As Ref. [43] lays out, surface sensors should detect the majority of energy deposited within a substrate if,

$$f_{\text{surf}} f_{\text{abs}} N_{\text{surf}} \sim 1, \quad (1)$$

where f_{surf} is the instrumented fraction of the substrate's surface, f_{abs} is the probability of absorption per interaction with the surface sensors, and N_{surf} is the number of said interactions. Average phonon sound speeds of $\text{km}\cdot\text{s}^{-1}$ and nominal lifetimes against anharmonic downconversion of $\mathcal{O}(10)$ ms, suggest $N_{\text{surf}} > 10^4$ for mm thick substrates. With $f_{\text{abs}} > 0.01$ even for $\mathcal{O}(10)$ nm thick aluminum on silicon (Al has a $1.6 \mu\text{m}$ pair-breaking length [41] and sound-speed mismatch limits the phonon transmittance to < 0.9), this suggests f_{surf} as low as a few % is sufficient for complete energy collection. Obviously, parasitic loss mechanisms must not unintentionally degrade the phonon lifetime and that substrate-absorber transmittance is high enough to not degrade f_{abs} . Maintaining these minimum values relies largely on proper engineering. Once the phonons have entered the film, a finite fraction of their energy is converted into quasiparticles. Simulation work of *photon* absorption in a thin-film superconductor suggest an upper bound of $\eta_{\text{pb}} \sim 0.60$ conversion fraction in the pair-breaking process [44, 45]. It is reasonable to assume a similar η_{pb} for phonons.

We can also parametrize the preceding discussion with a single *phonon-to-quasiparticle efficiency* η_{ph} [8],

$$\eta_{\text{ph}} = V\Delta\delta n_{\text{qp}}/E_{\text{dep}} \quad (2)$$

that helps directly translate from E_{dep} to the produced quasiparticle number $V\delta n_{\text{qp}}$. The literature on phonon-mediated detectors coupling sapphire or silicon substrates to aluminum absorbers yields $\eta_{\text{ph}} \sim 0.1\text{--}0.4$ [8, 46–50] as measured by low-threshold detectors. Cases for which $\eta_{\text{ph}} \ll \eta_{\text{pb}}$ are likely explained by phonon losses to mount points and inactive surface metal films ("dead metal").

We construct a simplified $n_{\text{qp}}(t)$ model with two time constants: a phonon absorption timescale τ_{abs} which characterizes how long $> 2\Delta$ phonons are present in the substrate to break pairs in the absorber films; and τ_{qp} , the recombination time constant in those films³ [32, 41, 51]. Literature measurements of τ_{qp} range from $0.1\text{--}10$ ms (for Al) [8, 52–55] depending on the quiescent quasiparticle density n_0 . Qubit and related superconducting systems report $n_0 \sim 0.1\text{--}1 \mu\text{m}^{-3}$ (e.g. Refs. [39, 56, 57]), which would correspond to $\tau_{\text{qp}} \gg$ ms for a standard generation-recombination model with Al recombination constant $R \approx 10 \mu\text{m}^3\text{s}^{-1}$ [58]. We assume a vanishing rise time for the phonon population, neglecting the time it

takes for the phonons produced by the energy deposition to become an approximately spatially homogeneous population in the substrate, because that rise time is only a few times the $\mathcal{O}(\mu\text{s})$ sound travel time for the considered substrates. Overall, solving the forced differential equation for our model with a single sensor (see Appendix A for specifics) results in a pulse model of the change in quasiparticle density:

$$\begin{aligned} \delta n_{\text{qp}}(t) &= \frac{N_{\text{qp}}^r}{V} \frac{\tau_{\text{qp}}}{\tau_{\text{abs}} - \tau_{\text{qp}}} \left(e^{-t/\tau_{\text{abs}}} - e^{-t/\tau_{\text{qp}}} \right) \\ N_{\text{qp}}^r &= \frac{\eta_{\text{ph}} E_{\text{dep}}}{\Delta} = \frac{E_{\text{abs}}}{\Delta}, \end{aligned} \quad (3)$$

where we have introduced N_{qp}^r as the maximum number of quasiparticles produced assuming a delta-function-like deposit of energy within the absorber, and E_{abs} as the intrinsic energy absorbed by the sensor factoring out the substrate.

The above prescription is modified slightly when using a junction island with a lower gap than the phonon absorber for quasiparticle trapping. Referring to [29, 59], the number of quasiparticles in the trap is related to the number in the absorber, assuming a phonon flux spatially homogeneous enough that the quasiparticle density in the absorber is uniform, by

$$N_{\text{trap}} \approx \eta_{\text{tr}} N_{\text{abs}} \eta_{\text{pb,tr}} \frac{\Delta_{\text{abs}}}{\Delta_{\text{tr}}}, \quad (4)$$

where η_{tr} is the fraction of quasiparticles in the absorber that become trapped, $\Delta_{\text{abs,tr}}$ are the absorber and trap gaps, and $\eta_{\text{pb,tr}}$ accounts for retention in the trap of the absorber quasiparticle energy as it is trapped and breaks Cooper pairs there. The trapping efficiency depends on the quasiparticle transmission probability into the trap, the "trapping time" τ_{tr} , the inverse of the rate at which a quasiparticle at Δ_{abs} loses enough energy to be trapped, typically by phonon emission, and the time the diffusing quasiparticle spends in the trap before exiting. Generally, only η_{tr} is experimentally measurable. For simplicity, we assume $\tau_{\text{tr}} \ll \tau_{\text{abs}}$ so it does not also need to be incorporated into Eq. 3. We make the approximation that all absorber quasiparticles entering the trap have energy Δ_{abs} , which is reasonable given how quickly excited quasiparticles decay to near Δ_{abs} by phonon emission [41]. Thus, we can modify Eq. 3 as,

$$N_{\text{qp}}^r = \eta_{\text{ph}} \eta_{\text{tr}} \eta_{\text{pb}} \frac{E_{\text{dep}}}{\Delta_{\text{tr}}}. \quad (5)$$

To close, we stress that the only fundamental limits in the above energy collection process are $\eta_{\text{ph}} < \eta_{\text{pb}}$ ($\eta_{\text{pb,abs}} \eta_{\text{pb,tr}}$ if trapping employed) and the limit on τ_{abs} from bulk anharmonic downconversion. All other efficiencies are amenable to design optimization (in particular limiting the amount of inactive absorbing material) or to material science study (surface-promoted phonon downconversion due to surface treatment).

³ These time constants may not be entirely independent: recombination phonons released into the substrate may be energetic enough and survive long enough to break pairs again, τ_{abs} may increase with τ_{qp} .

B. QPD Energy and Parity

The QPD Hamiltonian is described by the modified CPB Hamiltonian [60],

$$H_{\text{CPB}} = 4E_C \left(\hat{n} - n_g + \frac{P-1}{4} \right)^2 - E_J \cos \hat{\phi}, \quad (6)$$

where we have included the parity-dependent shift, $P = \pm 1$, to the offset charge n_g [61]. As is standard for a superconducting qubit, \hat{n} and $\hat{\phi}$ are conjugate operators corresponding to the number of Cooper pairs on the island and the phase difference across the junction, respectively. $E_J = \hbar\Delta/8R_N e^2$ is the Josephson energy, the barrier tunneling energy of Cooper pairs, with R_N the normal-state resistance of the junction. $E_C = e^2/2C_\Sigma$ is the charging energy interpretable as the energy required to shift the island charge by an electron. C_Σ is the total capacitance between the island and its circuit environment, formed from the sum of gate (C_g), junction (C_J), and shunt (C_s) capacitances (see Fig. 1). Following Ref. [61] a parity switch event, from $P = +1$ (even) to $P = -1$ (odd), shifts the offset charge by half of a Cooper pair and hence shifts the energy spectrum. This Hamiltonian is well studied, and solutions for a suggestive set of parameters are shown in Fig 4. We label the eigenstates of the CPB Hamiltonian by the state index $i = 0, 1, 2, \dots$ and charge parity terms $p = e, o$.

We consider two limits of the CPB Hamiltonian, corresponding to both styles of QPD, which are distinguished by the dominant energy scale: $\xi = E_J/E_C$. For a CPB, the use of a small (few fF) junction capacitance and the absence of shunt capacitance yield a large charging energy and $\xi \lesssim 1$. In the CPB limit, due to the curvature of the ground state, the difference between even and odd parity energy levels δE can be large and of the same order as E_J . For an OCS, a large $O(100 \text{ fF})$ shunt capacitor, added to flatten the energy levels in order to decrease sensitivity to environmental charge [22], results in a smaller charging energy and $\xi \gtrsim 1$. Note that only the lower energy levels are substantially flattened; the higher energy levels still exhibit a significant energy difference between even and odd states. Since our detector concept requires the even-odd difference in order for a change in island charge to be visible, we use these higher energy levels in the OCS case.

C. Quasiparticle Tunneling

For QPD operation, two characteristic tunneling rates are relevant: the rate for quasiparticles to tunnel into the island or pad, Γ_{in} , and the rate for quasiparticles to tunnel out of the island or pad, Γ_{out} . From symmetry considerations, assuming equal absorber sizes, an OCS QPD has $\Gamma_{\text{in}} = \Gamma_{\text{out}}$. Closed-form expressions can be calculated for Γ_{in} and Γ_{out} assuming that the density of non-equilibrium quasiparticles, δn_{qp} , is uniform throughout the absorber [14, 62, 63]. For typical device parameters, this approximation is justified since the quasiparticle diffusion timescale is much shorter than the quasiparticle tunneling or quasiparticle recombination timescales (see Appendix C). Under this assumption, one can define effective

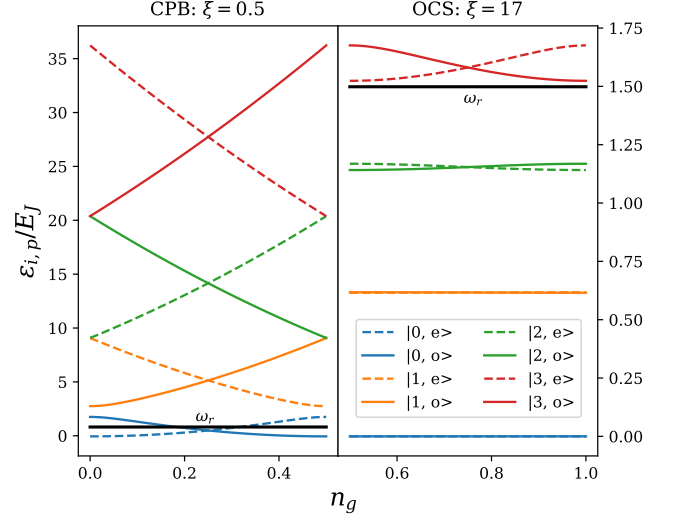


FIG. 4: Example energy level structure from solving the CPB Hamiltonian for CPB (Left) and OCS (Right) ξ ratios, with $E_J \sim 5$ GHz. The placement of the readout resonator is given by the black line.

chemical potentials for the more general case of the CPB with absorber and island [12] of $\delta\mu_{\text{abs, island}}$ (see Appendix B for specifics)

Using these effective chemical potentials, the rate for a thermalized quasiparticle to tunnel from the absorber to the island is given by Fermi's Golden Rule [12, 15, 63]:

$$\Gamma_{\text{in}} = \frac{16E_J}{h\Delta} \int_{\Delta}^{\infty} dE \frac{E(E + \delta E) - \Delta^2}{\sqrt{(E^2 - \Delta^2)[(E + \delta E)^2 - \Delta^2]} \times f(E - \delta\mu_{\text{abs}})[1 - f(E + \delta E - \delta\mu_{\text{island}})], \quad (7)$$

where $f(\epsilon)$ is the Fermi-Dirac distribution. The energy difference between odd and even parity for the ground state, δE , appears because the island voltage bias V_g renders the island a potential well of depth δE (for the electron component of an absorber quasiparticle), effectively shifting the energy spectrum of the island states δE below that of the absorber. Because $k_B T, \delta E \ll \Delta$, the Fermi level is well below Δ and the $1 - f(\epsilon)$ factor does not block tunneling: Γ_{in} is determined entirely by the absorber quasiparticle density, even in an OCS.

One key difference between CPB and OCS devices is that, in the CPB limit, the charging energy E_C is large (due to the small total capacitance) and $\delta E, E_C \gg E_J$. When a quasiparticle has tunneled to the island, the island energy spectrum shifts upward by δE and the lowest energy state for a quasiparticle on the island is occupied, blocking the tunneling of additional absorber quasiparticles [64] until the quasiparticle on the island tunnels out.

In an OCS, because $\delta E, E_C \ll E_J$, there is no such blockade, any number of quasiparticles can tunnel back and forth between absorbers, and thus $\Gamma_{\text{in}} = \Gamma_{\text{out}}$.

For the OCS case, we can move away from the integral form for Γ_{in} and work with the linearized form for small n_{qp} (see

Appendix B for derivation):

$$\Gamma_{\text{in}} \approx \frac{16E_J k_B T}{\mathcal{N} \Delta h} n_{\text{qp}} \equiv K n_{\text{qp}}. \quad (8)$$

Because the above form neglects δE , it is only approximately correct for the CPB case. Regardless, Γ_{in} is proportional to the quasiparticle density for both architectures. One can engineer the generic tunneling proportionality constant, K , by changing E_J , Δ , \mathcal{N} (the quasiparticle density of states defined in Appendix B), or δE if applicable.

Γ_{out} is more complicated for a CPB because of the aforementioned shift of the energy spectrum after tunneling has occurred. The island quasiparticle now has the same energy as the gap energy of the absorber, the energy it had before tunneling⁴. Therefore, one must calculate the “elastic” tunneling rate, which is valid more generally when quasiparticle tunnel out after tunneling in without first relaxing to a lower energy. Ref. [12]’s $\Gamma_{\text{out}}^{\text{el}}$ is the appropriate expression.

D. Readout Details

As is typical, we read out the charge-parity state of the QPD by capacitively coupling it to a superconducting resonator [15, 61] in the dispersive limit [35]. There is extensive experience with this approach in the literature for parity-state detection, particularly for QCDs [17, 18]. An alternative approach is to directly couple the CPB to the feedline, unmediated by a readout resonator [65]. While this approach has the benefit of simplicity and less dead metal (no readout resonator), the resonator approach decouples the qubit design (E_J and E_C , particularly) from requirements on the readout — the qubit can be optimized for energy sensitivity, and then the readout resonator adapted to the qubit design. Both approaches are under development, and practical experience will likely determine whether one approach is clearly better.

With a dispersive readout, the CPB Hamiltonian is far detuned from the resonator, preventing direct exchange of energy between the two systems [35]. Instead, the state of the CPB Hamiltonian shifts the resonant frequency of the readout resonator from its bare value by an amount $\chi_{i,p}(n_g)$ (for qubit state i and parity state P) which can be measured through a transmission measurement $S_{21}^{i,P}$.

The tunneling proportionality K from Sec. III C suggests that tunneling rates can approach for $O(100)$ kHz for reasonable shifts in quasiparticle density. In order for the resonator to readout such a high tunnel rate with good fidelity, the readout resonator’s signal bandwidth, f_r/Q_r , must be larger than the tunneling rate. A loaded quality factor of $O(10^4)$ dominated by the coupling ($Q_r \approx Q_c$), in a $O(\text{GHz})$ resonator, would meet said requirement by providing $O(\text{MHz})$ signal bandwidth.

A key difference between CPB and OCS style QPDs is the mechanism responsible for the shift in resonator frequency.

For CPBs, the existence of a strong relationship between gate charge and energy is interpretable as an effective quantum capacitance [15],

$$C_{i,p} = -\frac{C_g^2}{4e^2} \frac{\partial^2 \epsilon_{i,p}}{\partial n_g^2}. \quad (9)$$

The change in this parity-state-dependent capacitance $C_{i,p}$ shifts the readout resonator frequency [15]. The shift can be approximated in the reduced two-state Hilbert space case as,

$$C_{i=(0,1),p} \approx 4 \frac{C_g^2}{\xi C_\Sigma} \rightarrow \chi_{i=(0,1),p} \approx -\frac{1}{2} \omega_r^3 L_r C_{i=(0,1),p} \quad (10)$$

In the transmon regime ($\xi \gg 1$), Eq. 10 implies the quantum capacitance vanishes. Instead, the shift in ω_r is dominated by an alternative dispersive shift [61]. This $\chi_{i,p}$ can be derived from the full CPB-resonator Hamiltonian (see Ref. [66]) using second-order perturbation theory,

$$\chi_{i,p} = g^2 \sum_{j \neq i} \frac{2\omega_{ij,p} |\langle j, p | \hat{n} | i, p \rangle|^2}{\omega_{ij,p}^2 - \omega_r^2}, \quad (11)$$

where $\omega_{ij,p}$ is the transition frequency between transmon states $|i, p\rangle$ and $|j, p\rangle$, and g is the coupling between the transmon and the resonator. As with the Lamb Shift in atomic orbitals, photons in the readout resonator, even if not resonant with the qubit transitions, can be virtually absorbed and reemitted by the qubit, causing a shift in the energy of $|i, p\rangle$. Because of the denominator in Eq. 11, the effect is larger the closer the photon is to a qubit transition, and so we engineer the largest possible shift by placing ω_r close to an energy level difference $\omega_{j,p} - \omega_{i,p}$. We choose to place ω_r close to ϵ_{03} , as also shown in the right panel of Fig. 4.

Assuming reasonable parameters for various components, we can see $\chi_{i,p}(n_g)$ for the CPB and OCS in Fig. 5, along with the absolute difference in resonant frequency $\Delta\omega_r^i = (\chi_{i,e} - \chi_{i,o})$. We see that for ground state shifts, $\Delta\omega_r^{\text{max}}/2\pi = O(\text{MHz})$ for the CPB and $\Delta\omega_r^{\text{max}}/2\pi = O(100)$ kHz for the OCS. The CPB shift is of the same size as the FWHM and is eminently resolvable. While the OCS shift is smaller, the nominal frequency uncertainty of a thin-film superconducting resonator, read out at low power and limited by amplifier noise, is $O(100)$ Hz. [37, 38]. These shifts should be easily resolvable without special attention to readout strategy.

One complication in operating multiple QPDs on the same feedline (for use cases requiring pixelization) is that a gate bias value V_g will not match the optimal operating point for all sensors, due to inherent uncorrelated static charge drifts for each sensor. As Fig. 5 make clear, one needs to operate at half-integer n_g values corresponding to peaks. A potential solution is to *sweep* the bias in a similar fashion to Ref. [17]. Briefly, by ramping the bias in a sawtooth manner at a frequency f_{ramp} as shown in Fig. 6 Top, one traces through an entire cycle of n_g for all sensors. In an OCS QPD, tunneling events will break the smooth variation in $\chi_{i,p}$ and this effective phase shift is now the signature of a single tunneling event. The caveat

⁴ Because of the density of states singularity at Δ , it is reasonable to assume all non-equilibrium quasiparticles in the absorber reside at the gap energy

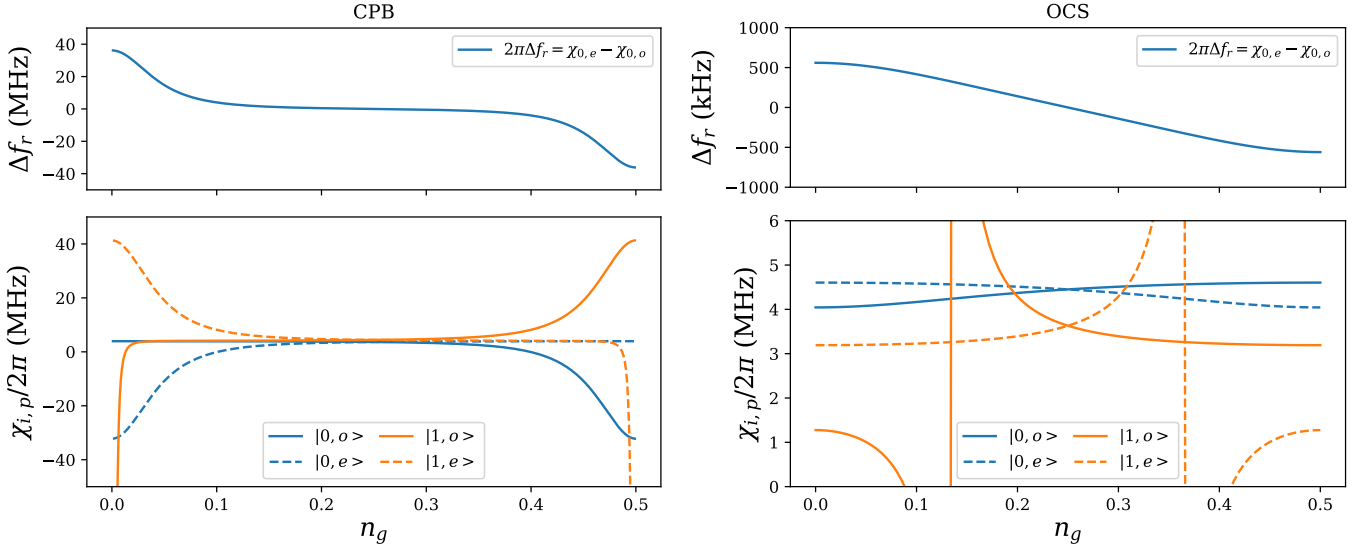


FIG. 5: *Top*: Absolute difference in resonator frequency between even and odd parity for the ground states of a CPB (*Left*) and OCS (*Right*). *Bottom*: Shift in resonator frequency of the ground and first excited state of a CPB due to the quantum capacitance shift (*Left*) and an OCS due to the dispersive shift (*Right*).

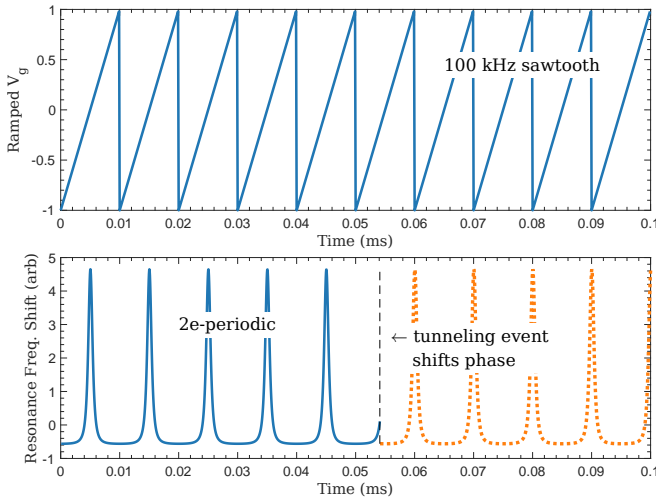


FIG. 6: *Top*: Example of a sawtooth voltage bias sweep at 100 kHz. *Bottom*: The stylized frequency shift expected when in the even state is given by the blue curve. A tunneling event in an OCS QPD effectively shifts the phase of this signal by shifting from the even \rightarrow odd curves and introducing a noticeable gap in the output signal.

is that large non-equilibrium quasiparticle densities, leading to tunneling rates $\Gamma_{\text{in/out}} \gg f_{\text{ramp}}$, will not be resolvable. A careful tuning of the resonator response speed is required to match expected signal tunneling rates. This technique is more complicated for CPB QPDs, as the relative energy level of a quasiparticle on the island is higher for $n_g = (0, 2e, \dots)$ [67] than in the absorber as the island depth δE flips sign with the changing n_g as seen in Fig. 3. At and near these points then, the small CPB island is effectively instantaneously cleared.

This behavior does not manifest for an OCS device as δE is negligible with increasing ξ . Thus, in a CPB QPD, such a rapid gate sweep will preferentially keep the device in the even state. However, episodes of rapid tunneling, such as after a burst of produced quasiparticles, will suppress peaks in the trace and produce “gaps” of one to a few peak widths in $\chi_{i,p}$ [17] before the periodic trace resumes. While the number of tunneling events cannot be ascertained from the presence of a gap, it can be used to tag discrete energy deposits that generated the rapid tunneling — potentially from single phonon absorption.

IV. DEVICE PERFORMANCE

Computing QPD performance, through modeling of expected signal and background rates, requires grappling with a variety of challenges — including the stochastic nature of the discrete parity transitions and asymmetric tunneling (at least in the case of the CPB) among other issues. To begin our discussion, we catalog expected fundamental and readout related noise sources in Sec. IV A. Next, we investigate a simplified device model in Sec. IV B, considering only OCS QPDs to get a flavor of expected performance metrics. Here we express our results in the more analytically tractable unit of number of transitions within a given period. Finally, Sec. IV C provides a more robust numerical modeling, using parity-state dwell-times instead and taking into account the effects of pulsing and asymmetric time-varying tunneling rates, and further discusses the factors that may affect our ability to disentangle signals from background.

For concreteness, we provide parameters for four hypothetical devices in Table I, investigating different pad material choices (aluminum vs hafnium) and device styles. The Hf case reflects an optimistic, yet plausible, scenario regarding

the use of a new material with favorable properties and thermal backgrounds. To avoid the confounding effect of the substrate, geometry-dependent η_{ph} , and phonon-to-film couplings, we deal with bounds only on the absorbed energy E_{abs} , which reflects intrinsic properties of the sensor.

Style	Aluminum		Hafnium	
	CPB	OCS	CPB	OCS
V	$100 \mu\text{m}^3$	$50 \mu\text{m}^3(\times 2)$	$1000 \mu\text{m}^3$	$500 \mu\text{m}^3(\times 2)$
T_c	1.2 K		0.25 K	
T_{opr}	0.1 K		0.025 K	
Δ	190 μeV		40 μeV	
E_{abs}	200 meV		40 meV	
n_0	$0.3 \mu\text{m}^{-3}$		$0.03 \mu\text{m}^{-3**}$	
E_J/h	4.9 GHz	6.14 GHz	4.9 GHz	6.14 GHz
E_C/h	11.1 GHz	356 MHz	11.1 GHz	356 MHz
ξ	0.5	17	0.5	17
Fano factor F	0.2			
τ_{qp}	1 ms [†]			
τ_{abs}	2 ms			
K	3 kHz $\cdot\mu\text{m}^3$		20 kHz $\cdot\mu\text{m}^3$	
Γ_{out}	2 kHz	n/a	10 kHz	n/a

TABLE I: Basic operating characteristics for device examples discussed in text with example E_{abs} . [†]Literature values of Hf thin-film quasiparticle lifetimes are $\sim 400 \mu\text{s}$ [68], though to our knowledge, and unlike Al, no serious R&D effort has been undertaken to extend this—which suggests significant improvement can be achieved in this frontier. ** Assuming thermal quasiparticles comprise the entirety of the quiescent background.

A. Noise Sources

Telegraph Noise: A pulse in the quasiparticle tunneling-in rate results in a two-state time-dependent charge-parity response in the QPD. This two-state flip-flop is referred to as a *telegraph* process. This telegraph noise represents noise *during* a pulse that may affect energy resolution at non-zero energy. For determining the threshold from the baseline (zero-energy) noise, we focus on the shot noise on the quiescent tunneling rates $\Gamma_{\text{in,out}}$, where the variance on the number of tunneling events in a given time period equals the expected mean number of tunneling events in that period.

Residual Quasiparticle Noise: For thin film aluminium, a quiescent (residual or steady-state) quasiparticle density of $n_0 = 0.01\text{--}1 \mu\text{m}^{-3}$ has been measured in qubit systems [39], with the population influenced by thermal or other pair-breaking processes [69]. We can account for the effect of this population by again modeling it as a super-Poissonian shot noise with variance proportional to the total quasiparticle number $\sigma^2 = 16n_0V$ (the prefactor comes from including pairing effects for phonon to quasiparticle breaking and recombination rates).

Fano Noise: For a given phonon energy deposit, the same number of quasiparticles will not always be generated. The process is not, however, Poissonian because of correlations

between the creation process for the quasiparticles. The sub-Poissonian nature is encoded in the Fano factor [70]. We include this contribution in our energy resolution modeling with $\sigma^2 = FN_{\text{qp}}^r$. As a first pass, we take F to be ≈ 0.2 [71], a number calculated for quasiparticle production from phonon absorption $\gg 2\Delta$. Its application to low energy phonon absorption will need to be experimentally validated.

System & Amplifier Noise: Amplifier noise can potentially limit the ability to observe parity transitions. The fractional frequency noise due to amplifier noise is given by [7],

$$\frac{\delta f}{f_r} \approx \sqrt{\frac{k_B T_N \Gamma_{\text{max}} Q_c}{2P_g Q_r^2}} \quad (12)$$

For conservative assumptions of noise temperature $T_N = 10$ K, feedline (readout) power of $P_g = -120$ dBm, coupling quality factor $Q_c = 10^4$ (\approx the loaded value Q_r), and a resonator bandwidth set in concordance with the maximum expected tunneling rate Γ_{max} of 1 MHz: the fractional frequency noise is 70 kHz. This is $\ll \Delta f_r$ from Sec. III D (even for the smaller shifts seen by the OCS style QPD).

TLS Noise: Two-level system (TLS) noise is often significant for thin-film superconducting resonators [38, 54]. TLS has also been seen to limit qubit coherence lifetimes [72]. We can calculate the impact of TLS noise in the same way as for amplifier noise: we integrate a typical TLS noise PSD [54, 73], $S_{df/f} \sim S_{df/f}(1 \text{ kHz/f})$ over a similar bandwidth Γ_{max} as for amplifier noise and find,

$$f_r \sqrt{S_{df/f} \Gamma_{\text{max}}} \sim 10 \text{ kHz}, \quad (13)$$

As in the case of amplifier noise, the RMS noise is much smaller than the parity flip signal and so does not factor into sensitivity.

B. Performance Estimates

We are now in a position to provide estimates for QPD performance. For a given time window $t_w = t_f - t_0$, the expected number of transitions S_w , can be computed as an inhomogeneous Poisson process by integrating the expected pulse shape,

$$S_w = \int_{t_0}^{t_f} K \delta n_{\text{qp}}(t) dt. \quad (14)$$

For our pulse model from Eq. 3, the total expected number of transitions from the entire pulse (with $t_w \gg \tau_{\text{abs,qp}}$) is,

$$S_{\text{avg}} = \frac{K}{V} N_{\text{qp}}^r \tau_{\text{qp}}. \quad (15)$$

We note the straightforward dependence on improving the tunneling proportionality (for instance by increasing E_J), decreasing the volume V (with the tradeoff of a smaller absorber area) and increasing τ_{qp} .

A simple expression for the stochastic background can be obtained by defining the random variables:

$$\begin{aligned} N_0 &\sim \text{Gaussian}(N_0, \sigma = 4\sqrt{N_0}) \\ B &\sim \text{Poisson}(B_{\text{avg}} = \frac{Kt_w}{V}N_0), \end{aligned} \quad (16)$$

with N_0 the quiescent quasiparticle population (in quasiparticle number units) and B is the background number of transitions within the window, taking into account the telegraph shot noise. Note that B is a mixture distribution. In the limit of a large number of transitions we can treat B as a Gaussian process, which allows us to write the variance in the background distribution as the distributed product,

$$\begin{aligned} \sigma_{B_{\text{tot}}}^2 &= \sigma_{N_0}^2 \left(\frac{dB}{dN_0} \right)^2 + \sigma_B^2 \\ &= \left(Kt_w + 16 \frac{K^2 t_w^2}{V} \right) n_0. \end{aligned} \quad (17)$$

The signal variance can be written in a similar way, including the telegraph and Fano components, as:

$$\begin{aligned} N_F &\sim \text{Gaussian}(N_{\text{qp}}^r, \sigma_F = \sqrt{FN_{\text{qp}}^r}) \\ S &\sim \text{Poisson}\left(\frac{K\tau_{\text{qp}}}{V}N_F\right). \end{aligned} \quad (18)$$

As we are interested in a sensitivity estimate here, we elide the changing transition rate due to the varying pulse shape and use only the overall number of transitions from Eq. 15. Treating S as Gaussian for tractability we have,

$$\sigma_S^2 = \left(K \frac{\tau_{\text{qp}}}{V} + K^2 \left(\frac{\tau_{\text{qp}}}{V} \right)^2 F \right) N_{\text{qp}}^r. \quad (19)$$

From the parameters in Table I we have the results shown in Table II. We have used Eq. 15 to convert σ_B into a “ 5σ ” thresh-

	Aluminum	Hafnium
S_{avg}	20	13
$B_{\text{avg}} \equiv \langle B \rangle$	3.6	2.4
$\sigma_{B_{\text{tot}}}$	2.0	1.6
σ_S	8.9	7.1
$E_{\text{abs}} \text{ threshold (meV)}$	165	37

TABLE II: Expected signal & background transition counts and resolvable absorbed energy threshold for OCS style devices, from example parameters provided in Table I, for a window $t_w = 3\tau_{\text{abs}}$.

old, the minimum energy deposit potentially resolvable from background. The values, particularly for the larger Hf device and extrapolating downward in volume, reflect the potential to resolve single phonon events.

The observant reader might argue that the absorber surface sizes (for 50 nm thick metal) inferred from Table I suggest fill fractions f_{surf} in Eq. 1 that are $\ll 1\%$ for cm^2 substrates, implying $\eta_{\text{ph}} \ll \eta_{\text{pb}}$ and driving up E_{dep} thresholds. For instance $\eta_{\text{ph}}=0.01$ would give an E_{dep} threshold of 1.5 eV even

in the case of the Hf device. However, as discussed in Sec. III A, improvements to absorbed phonon energy can likely be made by mitigating phonon loss mechanisms. Additionally, it is worth considering the trapping and multiplication geometry broached in Sec. II and Fig. 2. The crucial point is that it is the volume of the trap and *not* the absorber that sets the tunneling proportionality K . Thus, the scaling relation between absorber volume and K is broken. Referring back to Eq. 4 we note from the literature that η_{tr} can be engineered to be ≈ 0.2 [59, 74, 75] for $O(0.1) \text{ mm}^2$ aluminium absorbers with tungsten traps. Assuming a similarly achievable regime for our Al/Hf design yields $N_{\text{trap}} \approx O(1) \cdot N_{\text{abs}}$. Thus, the number of quasiparticles produced in the much smaller Hf trap is similar to that within the Al absorber.

Care needs to be taken to account for the quiescent quasiparticle density in the absorber and its effect on the quasiparticle density in the trap. Non-thermal mobile background quasiparticles created in the absorber, such as through a constant source of background IR radiation [58], may significantly impact the density in the trap because the trap acts as a sink. We can estimate the size of this effect using a simple balance model (see Appendix D) that factors in generation, recombination, and trapping. For a seemingly negligible excess density of $n_0 = 0.05 \mu\text{m}^{-3}$ in a reasonably sized Al absorber of $\sim 16000 \mu\text{m}^3$ ($575 \mu\text{m} \times 575 \mu\text{m} \times 50 \text{ nm}$, fulfilling the f_{surf} requirement for a cm^2 substrate), a $100 \mu\text{m}^3$ Hf trap would have a much higher (than purely thermal origin) quasiparticle density of $n_0^{\text{trap}} \sim 0.25 \mu\text{m}^{-3}$. These numbers suggest a *deposit* resolution and threshold for that system of,

$$\sigma_{\text{dep}} \approx 50 \text{ meV} \rightarrow E_{\text{dep}}^{\text{threshold}} \approx 250 \text{ meV} \quad (20)$$

It will be crucial to drive down n_0 in the absorber to the thermal floor. In such a condition, the dominant background will again be the thermal density within the trap alone. For an operating temperature of $T = 0.025 \text{ K}$ (and effectively no thermal quasiparticles in the absorber), this leads to a deposit resolution of,

$$\sigma_{\text{dep}} \approx 15 \left(\frac{V_{\text{trap}}}{100 \mu\text{m}^3} \right)^{\frac{1}{2}} \text{ meV}. \quad (21)$$

Such a design would immediately allow for the sensing of single optical phonons and the high-tail of acoustic phonons. Optimization of the trap volume down to a few μm^3 with corresponding improvements in trapping efficiency (e.g. by funneling quasiparticles more efficiently) would result in a threshold of just a few meV, with the ability to probe for signals from single acoustic phonons. All told, these calculations demonstrate the potential to detect and reconstruct $\ll \text{eV}$ substrate energy deposits, providing a path to sensitivities well beyond currently demonstrated technologies [6, 7].

C. Energy Reconstruction & Thresholds

Having covered a basic model of the signal and noise, we are ready to work through more concrete, numerically simulated performance metrics. We simulate the two-state, parity

signal of a QPD in response to an energy deposit, folding in the fundamental noise sources discussed in the previous section. We consider the case of a device consisting of a single superconducting material and discuss sensitivity on E_{abs} , restricting ourselves to only the intrinsic sensor physics. These results can heuristically be extended to E_{dep} by factoring in η_{ph} by hand in the case of a single material device or by using the Eq. 4 prescription for a scenario making use of two materials and quasiparticle trapping.

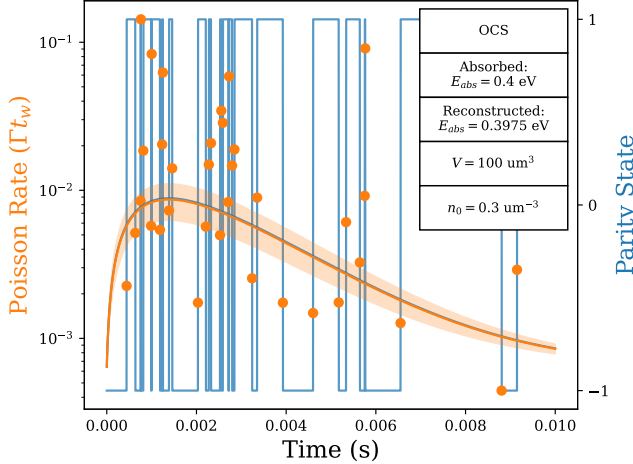


FIG. 7: Simulated parity state time-series (blue telegraph signal) for parameters given in inset. Dwell times points derived from this trace, converted to an equivalent transition rate, are given as the orange circles. The pulse reconstruction is shown by the orange line, with the shaded band corresponding to 1σ on the reconstructed energy.

We start by discretizing pulses (defined by Eq. 3) and their time-spans into bins of width t_w , assuming a sampling frequency faster than the resonator response and maximum expected tunneling rate. Next, for each time bin, we sample a Poisson distribution to determine whether parity-state transitions occur in the given interval. The choice of sampling frequency will be crucial in any experimental realization, to ensure that the probability of more than one transition occurring in a window is negligible. The relevant Poisson parameter depends on both the current parity state, and whether the device is a CPB or OCS:

$$\lambda_{\text{even}} = S_w(\mathbf{N}_F) + B_{\text{avg}}$$

$$\lambda_{\text{odd}} = \begin{cases} \lambda_{\text{even}} & \text{OCS} \\ \Gamma_{\text{out}} t_w = \text{constant} & \text{CPB} \end{cases}$$

where $S_w(\mathbf{N}_F)$ should be interpreted as initially sampling \mathbf{N}_F from Eq. 18, fixing that result as N_{qp}^r in Eq. 3, and subsequently computing S_w from Eq. 14. From this process we can construct a telegraph signal time-series of transitions, an example of which is shown by the blue curve in Fig. 7.

To reconstruct a pulse, we first convert its telegraph signal to a series of even and odd state dwell times, $\delta t_{e,o}$, defined as how long the system stayed at its last parity until a transition

occurred. We then estimate the Poisson parameter at each bin a flip occurs, as:

$$\hat{\lambda}_{\text{even, odd}} = \frac{t_w}{\delta t_{e,o}}$$

This prescription provides us with a series of points in time that are samples of the true transition rate, seen as the orange points in Fig. 7. We can fit this data with a 2 parameter model ($\delta n_{\text{qp}}, n_0$) incorporating the expected pulse shape and quiescent quasiparticle density, with results shown as the orange best-fit line in the figure. For this simulation, we assume we know the pulse start time, while a more complete simulation would fit that as a free parameter (and accept the corresponding impact on threshold).

There are a few subtleties that depend on the value of ξ . Because tunneling in is blocked when the CPB is in the odd state, the total number of observed qubit state transitions in any interval will be a factor of roughly $2\Gamma_{\text{out}}/(\Gamma_{\text{in}} + \Gamma_{\text{out}})$ fewer in the CPB case (for equivalent Γ_{in}). Furthermore, since the OCS tunneling is bi-directional, both even and odd dwell times provide information about the quasiparticle density whereas in the CPB only Γ_{in} is proportional to quasiparticle density.

We can repeat this simulation thousands of times to explore the parameter space summarized in Table I. For the listed values, Fig. 8 shows reconstructed E_{abs} values and thresholds. The shaded bands reflect the 1σ deviation in reconstruction. For regions where the distribution of reconstructed events is non-normal, such as at zero to low energies, we instead compute 1σ -equivalent quantiles. We infer “ 5σ ” thresholds from the baseline resolution reconstructed from simulations with no energy deposit. We note the consistency between these thresholds and the back-of-the-envelope values from Sec. IV B. For sufficiently low E_{abs} , the residual quasiparticle density n_0 sets the threshold. At the high end, the primary factor driving saturation in both sensor modalities is when the tunneling rate exceeds the resonator bandwidth, $\Gamma_{\text{in}} > Q_r/\tau_r\pi$, and one cannot accurately reconstruct the number of transitions due to the slow resonator response. This suggests that the resonator should be designed to accommodate the typical tunneling rate, perhaps at a cost in Q_r and thus in signal-to-noise for the parity flip relative to amplifier noise.

The relative low-energy baseline thresholds of the OCS and CPB schemes are comparable (and almost identical for the AI device due to judiciously chosen parameters) perhaps suggesting that the CPB, having a larger χ_{ij} shift and simpler design, is preferable. However, the situation is not straightforward as we see the larger reconstruction variance along CPB curves in Fig. 8 — primarily due to Γ_{out} being constant for the CPB, along with having a fewer number of transitions for an equivalent energy deposit. Additionally, as Fig. 9 indicates, the CPB threshold degrades dramatically with increasing n_0 as compared to the OCS. Their performance is only similar when $\Gamma_{\text{in}} < \Gamma_{\text{out}}$. It should be noted that at high enough n_0 both modalities will experience a degradation in sensitivity due to saturation effects, with the OCS likely paying the penalty earlier due to always having more transitions in an interval and thus saturating faster. The overall dependence on volume is as expected: a smaller volume provides a higher signal quasipar-

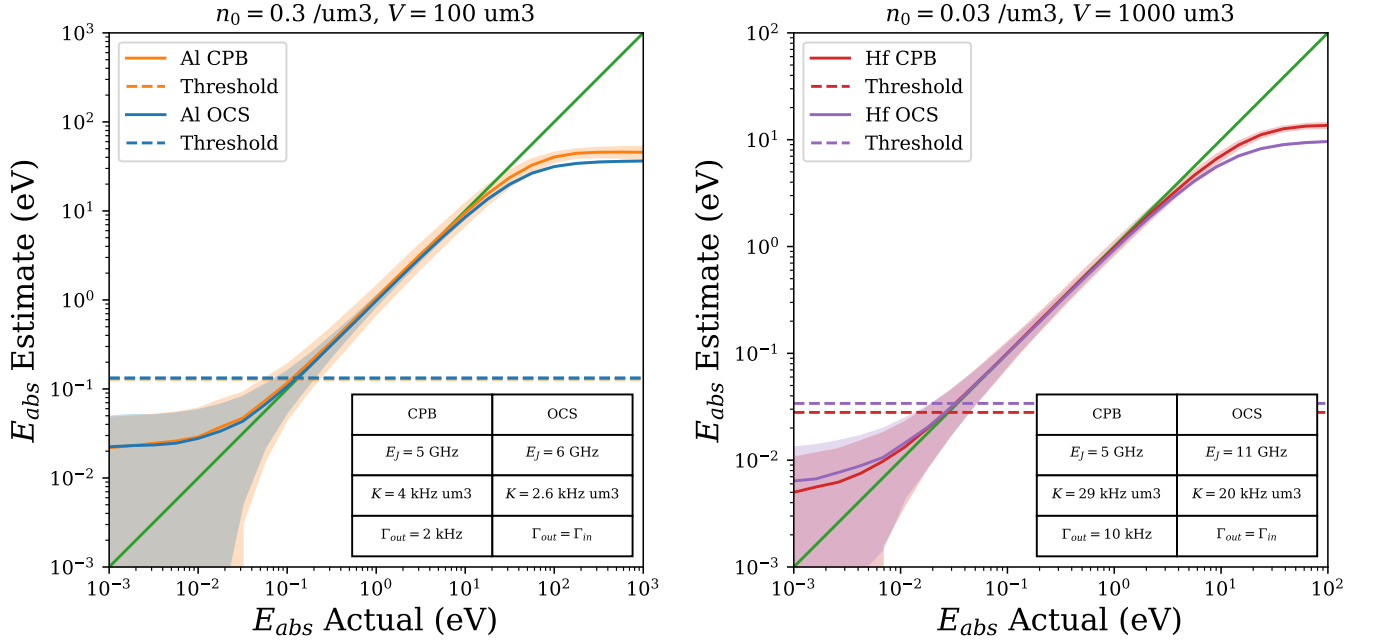


FIG. 8: *Left*: Reconstructed energy estimate vs simulated energy deposit for Aluminum CPB & OCS sensors with 100 um^3 total absorber volume. *Right*: Similar curves Hf devices with 1000 um^3 total volume of absorber. 1σ equivalent quantiles are given by the shaded bands, with energy thresholds (described in text) shown as the dotted lines.

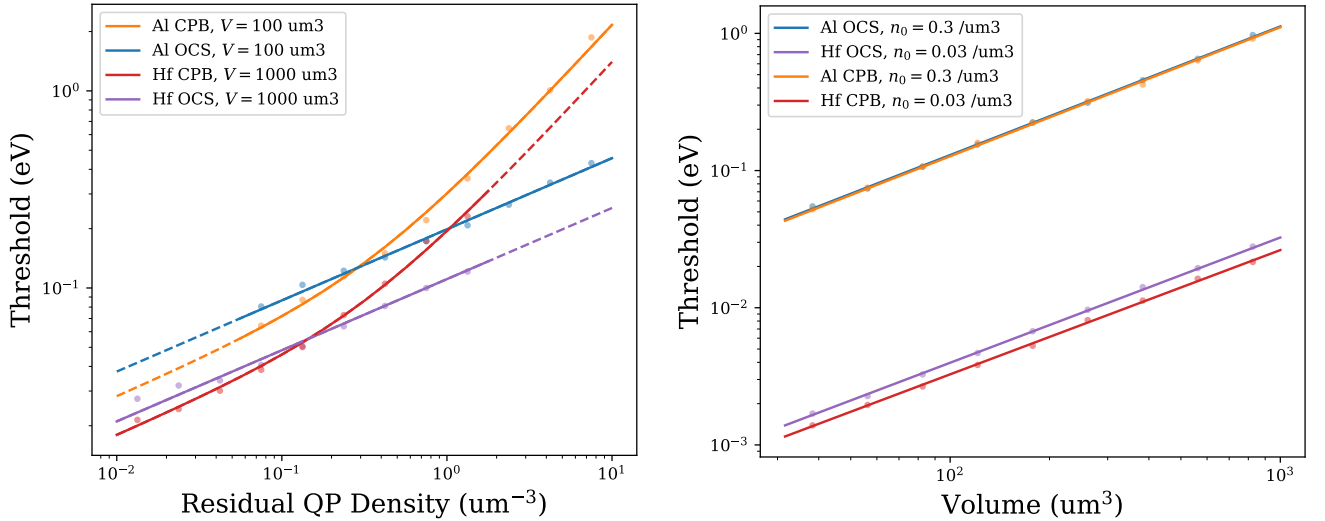


FIG. 9: *Left*: Simulated effect of quiescent quasiparticle density on E_{abs} threshold. n_0 is simulated in the neighborhood of Table I values and extrapolated based on expected behavior elsewhere. *Right*: Simulated volume dependence on E_{abs} threshold.

ticle density for a given energy deposit, though this calculation neglects any potential related changes in phonon collection efficiency. Also as expected, Hf offers lower threshold at the same n_0 than Al because of the higher quasiparticle yield per unit energy deposit. An increase in n_0 with decreasing Δ could counter this gain. In total then, both QPD styles are attractive candidates for phonon mediated sensing.

D. Additional Considerations

In the preceding sections, we demonstrated that, for a reasonable set of assumptions and parameters, the QPD offers potentially ground-breaking energy threshold for phonon-mediated particle detection. A development program would begin with single-material devices to establish basic experimental parameters followed likely by two-material devices incorporating quasiparticle trapping. Many choices must be

made and challenges overcome, however, which we delineate here:

Material Selection: There are a plethora of low T_C (< 1 K) superconducting materials, including alloys, that are suitable for thin film applications — including W, AlMn, Ir, IrPt, Os, and Ti [31, 76]. Workable tunnel junctions have not been convincingly demonstrated with most of these materials. Quasi-particle lifetime, phonon acoustic mismatch and collection, and amenability to device fabrication not been exhaustively investigated. R&D on these and other lower-gap materials is warranted given the potential gain in responsivity.

Volume & Diffusion: We have already discussed the effects of absorber/trap sizing and volume on tunneling rates in Sec. IV. However, the discussion there uses the shorthand of chemical potentials — convincingly used in the original QCD detector papers to demonstrate the linearity of the tunneling rate — while a more complete modeling would take into account the dynamic quasiparticle drift and diffusion processes. Those topics are, however, fraught with uncertainty, as briefly discussed in Appendix C, with varying literature reported values for diffusion coefficients and its dependence on temperature, film thickness, and gap [42, 74, 75, 77, 78]. Experimental verification, through direct measurement of QPD response, will prove crucial for determining future optimizations of absorber shape and sizing.

Quasiparticle Cascade and Trap Design: As exhaustively studied in the CDMS dark matter direct-detection experimental program (e.g. see Refs. [32, 40, 79] for these spanning two decades), efficiently collecting quasiparticles within a constrained region, in absorber→trap designs, will be of paramount importance in maximizing phonon sensitivity. Choices of absorber and trap lengths, material thicknesses, and overlap fractions will have to be simulated and tuned to achieve meV-scale E_{dep} thresholds. It is also imperative that n_0 be sufficiently low in the absorber, otherwise the absorber may significantly elevate the trap background level.

Vortices & Quasiparticle Trapping: Ref. [80] discusses the impact of pinned (trapped) magnetic vortices, areas of quantized flux circulation. The local gap in these regions is driven to 0, and this sink-like behavior traps quasiparticles. Thus, pinned vortices in the QPD absorber could prevent quasiparticles from reaching the junctions. Ref. [80] notices the geometrical dependence on pad shape for the vortex contribution, suggesting this might be one avenue to reduce their importance. Furthermore, very high magnetic permeability shielding could be used to prevent vortices from forming in the first place [81].

Phonon Loss Simulations: Non-sensitive, phonon absorbing dead-metal on the substrate (e.g. the feedline) likely poses a significant challenge to maximizing η_{ph} . Any phonon losses directly degrade the energy resolution of the QPD. As discussed in Sec. III A, literature values for η_{ph} vary widely between different experiments, making accurate determination of this parameter of vital importance. One promising avenue for accurate modeling is through use of bespoke phonon simulation software like G4CMP [82], with recent examples of phonon absorption simulations having been conducted for Kinetic Inductance Detectors [83] and qubits [20]. Experimental

techniques to reduce phonon loss could include suspending the substrate via hanging wirebonds [84] or in flip-chip designs where the ground plane and readout scheme are physically decoupled from the substrate [85, 86].

Direct Feedline Coupling: The demonstrated parity counting experiment in Ref. [65] of a feedline coupled transmon does away with the readout resonator entirely. The clear benefit of such an approach would be in reducing resonator associated inactive metal, mitigating phonon losses as discussed previously. However, the very low readout powers ($\lesssim -140$ dBm) required for this mode of operation, along with the potential for unwanted, readout-power-generated quasiparticles seen in other superconducting systems [87], requires careful design work to implement.

V. APPLICATION TO A RARE-EVENT SEARCH AND CONCLUSION

To get a flavor of the science reach of QPDs, and with the performance curves of Sec. IV C in mind, we can consider their ability to probe for a light dark matter particle (mass m_χ) elastically scattering off a much heavier target (i.e. a silicon atom with mass m_T) [3]. From basic kinematics, the maximum energy transfer in such a two-body collision, if $m_T \gg m_\chi$, is $E_{\text{max}} \approx 2m_\chi^2 v_\chi^2 / m_T$. The dark matter velocity v_χ is constrained to be the Milky-Way escape velocity of ~ 600 km/s. Assuming all of E_{max} makes its way into the absorber (factoring in $\eta_{\text{ph}} \sim 30\%$), a mixed Al/Hf device with a 75 meV deposit threshold could probe down to $m_\chi \sim 10$ MeV c^{-2} . Current experimental constraints for such elastically scattering light dark matter become weak at $m_\chi \sim 100$ MeV c^{-2} [88, 89]. Thus, QPDs could provide an order-of-magnitude improvement in probing light dark matter parameter space.

In summary, we have outlined a novel scheme of using qubit derived sensors for rare-event search particle physics applications. We have described the relevant physics and operating principles for these Quantum Parity Detectors along with preliminary calculations for potential noise sources and detector sensitivity. We have argued that such devices are intrinsically able to detect 10s of meV energy deposits and, given further R&D into substrate-device couplings, should eventually be able sense single substrate-phonon events of a similar magnitude. QPDs could therefore be an excellent match to the challenge of detecting the lightest fermionic dark matter candidates. Ongoing fabrication efforts, based on designs presented in this paper, will hopefully experimentally verify the validity of the proposed schemes and calculations presented.

ACKNOWLEDGMENTS

We thank SLAC and FNAL collaborators for insightful conversations regarding qubits, phonons, and quasiparticles. This research was primarily supported by National Science Foundation PHY Grant 2209581 and the Schwartz/Reisman Collaborative Science Program between Caltech and the Weizmann Institute of Science. KR was supported in part by a Caltech

Prize Postdoctoral Fellowship and JP by the Caltech SURF Program. This work was conducted at the California Institute

of Technology, NASA's Jet Propulsion Laboratory, and the Weizmann Institute of Science.

-
- [1] M. Battaglieri *et al.*, [arXiv:1707.04591 \[hep-ph\]](#) (2017), and references therein; R. Kolb, H. Weerts, N. Toro, R. Van de Water, R. Essig, D. McKinsey, K. Zurek, A. Chou, P. Graham, J. Estrada, *et al.*, *Basic research needs for dark-matter small projects new initiatives: Report of the Department of Energy's high energy physics workshop on dark matter*, Tech. Rep. (USDOE Office of Science (SC)(United States), 2018); B. Fleming, I. Shipsey, M. Demarteau, J. Fast, S. Golwala, Y.-K. Kim, A. Seiden, J. Hirschauer, G. Sciolla, O. Palamara, *et al.*, *Basic Research Needs for High Energy Physics Detector Research & Development: Report of the Office of Science Workshop on Basic Research Needs for HEP Detector Research and Development: December 11-14, 2019*, Tech. Rep. (USDOE Office of Science (SC)(United States), 2019).
- [2] D. K. Papoulias, T. S. Kosmas, and Y. Kuno, *Frontiers in Physics* **7**, 191 (2019).
- [3] R. Essig, G. K. Giovanetti, N. Kurinsky, D. McKinsey, K. Ramanathan, K. Stifter, T.-T. Yu, A. Aboubrahim, D. Adams, D. Alves, *et al.*, [arXiv preprint arXiv:2203.08297](#) (2022).
- [4] T. Trickle, *Direct Detection of Light Dark Matter with Electrons, Phonons, and Magnons* (California Institute of Technology, 2022).
- [5] K. D. Irwin, S. W. Nam, B. Cabrera, B. Chugg, and B. A. Young, *Review of Scientific Instruments* **66**, 5322 (1995).
- [6] J. Rothe, G. Angloher, P. Bauer, A. Bento, C. Bucci, L. Canonica, A. D'Addabbo, X. Defay, A. Erb, F. v. Feilitzsch, *et al.*, *Journal of Low Temperature Physics* **193**, 1160 (2018); I. Alkhatib, D. Amaral, T. Aralis, T. Aramaki, I. J. Arnquist, I. A. Langroudy, E. Azadbakht, S. Banik, D. Barker, C. Bathurst, *et al.*, *Physical Review Letters* **127**, 061801 (2021); C. Fink, S. Watkins, T. Aramaki, P. Brink, S. Ganjam, B. Hines, M. Huber, N. Kurinsky, R. Mahapatra, N. Mirabolfathi, *et al.*, *AIP Advances* **10** (2020); R. Romani, [Correlated and uncorrelated backgrounds and noise sources in athermal phonon detectors and other low temperature detector](#) (2023).
- [7] O. Wen, T. Aralis, R. Basu Thakur, B. Bumble, Y.-Y. Chang, K. Ramanathan, and S. Golwala, *Journal of Low Temperature Physics* **209**, 510 (2022).
- [8] D. Moore, S. Golwala, B. Bumble, B. Cornell, P. Day, H. LeDuc, and J. Zmuidzinas, *Applied Physics Letters* **100** (2012); D. Delicato, A. Ahmad, L. Bandiera, M. Calvo, M. Cappelli, G. Del Castello, M. Roccagiovine, M. Giammei, V. Guidi, D. Maiello, *et al.*, [arXiv preprint arXiv:2308.14399](#) (2023).
- [9] Y. Nakamura, Y. A. Pashkin, and J. Tsai, *nature* **398**, 786 (1999); A. Somoroff, Q. Ficheux, R. A. Mencia, H. Xiong, R. Kuzmin, and V. E. Manucharyan, *Physical Review Letters* **130**, 267001 (2023).
- [10] C. D. Wilen, S. Abdullah, N. Kurinsky, C. Stanford, L. Cardani, G. d'Imperio, C. Tomei, L. Faoro, L. Ioffe, C. Liu, *et al.*, *Nature* **594**, 369 (2021).
- [11] V. Iaiia, J. Ku, A. Ballard, C. Larson, E. Yelton, C. Liu, S. Patel, R. McDermott, and B. Plourde, *Nature Communications* **13**, 6425 (2022); A. Bargerbos, L. J. Splithoff, M. Pita-Vidal, J. J. Wesdorp, Y. Liu, P. Krogstrup, L. P. Kouwenhoven, C. K. Andersen, and L. Grünhaupt, *Physical Review Applied* **19**, 024014 (2023); J. M. Martinis, *npj Quantum Information* **7**, 90 (2021); M. McEwen, K. C. Miao, J. Atalaya, A. Bilmes, A. Crook, J. Bovaird, J. M. Kreikebaum, N. Zobrist, E. Jeffrey, B. Ying, *et al.*, [arXiv preprint arXiv:2402.15644](#) (2024).
- [12] M. D. Shaw, R. M. Lutchyn, P. Delsing, and P. M. Echternach, *Physical Review B* **78**, 024503 (2008), publisher: American Physical Society.
- [13] G. Catelani, *Physical Review B* **89**, 094522 (2014).
- [14] G. Catelani, R. J. Schoelkopf, M. H. Devoret, and L. I. Glazman, *Physical Review B* **84**, 064517 (2011).
- [15] M. D. Shaw, J. Bueno, P. Day, C. M. Bradford, and P. M. Echternach, *Physical Review B* **79**, 144511 (2009).
- [16] J. Bueno, M. Shaw, P. Day, and P. Echternach, *Applied Physics Letters* **96** (2010).
- [17] P. M. Echternach, B. J. Pepper, T. Reck, and C. M. Bradford, *Nature Astronomy* **2**, 90 (2018).
- [18] P. M. Echternach, A. D. Beyer, and C. M. Bradford, *Journal of Astronomical Telescopes, Instruments, and Systems* **7**, 011003 (2021).
- [19] C. W. Fink, C. Salemi, B. A. Young, D. I. Schuster, and N. A. Kurinsky, [arXiv preprint arXiv:2310.01345](#) (2023).
- [20] R. Linehan, I. Hernandez, D. J. Temples, S. Q. Dang, D. Baxter, L. Hsu, E. Figueroa-Feliciano, R. Khatiwada, K. Anyang, D. Bowring, G. Bratrud, G. Cancelo, A. Chou, R. Gualtieri, K. Stifter, and S. Sussman, Estimating the energy threshold of phonon-mediated superconducting qubit detectors operated in an energy-relaxation sensing scheme (2024), [arXiv:2404.04423 \[physics.ins-det\]](#).
- [21] K. Serniak, M. Hays, G. De Lange, S. Diamond, S. Shankar, L. Burkhart, L. Frunzio, M. Houzet, and M. Devoret, *Physical Review Letters* **121**, 157701 (2018).
- [22] J. Koch, M. Y. Terri, J. Gambetta, A. A. Houck, D. I. Schuster, J. Majer, A. Blais, M. H. Devoret, S. M. Girvin, and R. J. Schoelkopf, *Physical Review A* **76**, 042319 (2007).
- [23] S. Knappen, T. Lin, M. Pyle, and K. M. Zurek, *Physics Letters B* **785**, 386 (2018).
- [24] R. Essig, M. Fernandez-Serra, J. Mardon, A. Soto, T. Volansky, and T.-T. Yu, *Journal of High Energy Physics* **2016**, 1 (2016).
- [25] A. Shnirman, G. Schön, and Z. Hermon, *Physical Review Letters* **79**, 2371 (1997).
- [26] Y. Y. Gao, M. A. Rol, S. Touzard, and C. Wang, *PRX Quantum* **2**, 040202 (2021).
- [27] S.-H. Kim, H.-S. Jeong, K. Kiuchi, S. Kanai, T. Onjo, K.-i. Takemasa, Y. Takeuchi, H. Ikeda, S. Matsuura, H. Sato, *et al.*, *Physics Procedia* **37**, 667 (2012).
- [28] S. Kraft, A. J. Peacock, M. Bavdaz, B. Castelletto, B. Collaudin, D. Perez, R. Venn, and T. E. Harper, in *EUV, X-Ray, and Gamma-Ray Instrumentation for Astronomy IX*, Vol. 3445 (SPIE, 1998) pp. 226–235.
- [29] N. Booth, *Applied physics letters* **50**, 293 (1987).
- [30] D. Goldie, N. Booth, C. Patel, and G. Salmon, *Physical Review Letters* **64**, 954 (1990).
- [31] T. Saab, R. Clarke, B. Cabrera, R. Abusaidi, and R. Gaitskell, *Nuclear Instruments and Methods in Physics Research Section A: Accelerators, Spectrometers, Detectors and Associated Equipment* **444**, 300 (2000).
- [32] M. C. Pyle, *Optimizing the design and analysis of cryogenic semiconductor dark matter detectors for maximum sensitivity* (Stanford University, 2012).

- [33] A. Wallraff, D. I. Schuster, A. Blais, L. Frunzio, R.-S. Huang, J. Majer, S. Kumar, S. M. Girvin, and R. J. Schoelkopf, *Nature* **431**, 162 (2004).
- [34] J. Q. You and F. Nori, *Physics Today* **58**, 42 (2005), arXiv: quant-ph/0601121.
- [35] P. Krantz, M. Kjaergaard, F. Yan, T. P. Orlando, S. Gustavsson, and W. D. Oliver, *Applied Physics Reviews* **6**, 021318 (2019), arXiv: 1904.06560.
- [36] J. Aumentado, M. W. Keller, J. M. Martinis, and M. H. Devoret, *Physical Review Letters* **92**, 066802 (2004).
- [37] J. Burnett, A. Bengtsson, D. Niepce, and J. Bylander, in *Journal of Physics: Conference Series*, Vol. 969 (IOP Publishing, 2018) p. 012131.
- [38] K. Ramanathan, O. Wen, T. Aralis, R. B. Thakur, B. Bumble, Y.-Y. Chang, P. K. Day, B. H. Eom, H. G. LeDuc, B. J. Sandoval, *et al.*, arXiv preprint arXiv:2402.05419 (2024).
- [39] T. Connolly, P. D. Kurilovich, S. Diamond, H. Nho, C. G. L. Bøttcher, L. I. Glazman, V. Fatemi, and M. H. Devoret, *Coexistence of nonequilibrium density and equilibrium energy distribution of quasiparticles in a superconducting qubit* (2023), arXiv:2302.12330 [cond-mat, physics:quant-ph].
- [40] T. Saab, *Search for weakly interacting massive particles with the Cryogenic Dark Matter Search experiment* (stanford university, 2002).
- [41] S. B. Kaplan, C. C. Chi, D. N. Langenberg, J. J. Chang, S. Jafarey, and D. J. Scalapino, *Physical Review B* **14**, 4854 (1976).
- [42] C. W. Fink, *A Gram-Scale low-T c Low-Surface-Coverage Athermal-Phonon Sensitive Dark Matter Detector* (University of California, Berkeley, 2022).
- [43] S. R. Golwala and E. Figueroa-Feliciano, *Annual Review of Nuclear and Particle Science* **72**, 419 (2022).
- [44] T. Guruswamy, D. Goldie, and S. Withington, *Superconductor Science and Technology* **27**, 055012 (2014).
- [45] A. Kozorezov, A. Volkov, J. Wigmore, A. Peacock, A. Poelaert, and R. Den Hartog, *Physical Review B* **61**, 11807 (2000).
- [46] D. J. Temples, O. Wen, K. Ramanathan, T. Aralis, Y.-Y. Chang, S. Golwala, L. Hsu, C. Bathurst, D. Baxter, D. Bowring, *et al.*, arXiv preprint arXiv:2402.04473 (2024).
- [47] R. Ren, C. Bathurst, Y. Chang, R. Chen, C. Fink, Z. Hong, N. Kurinsky, N. Mast, N. Mishra, V. Novati, *et al.*, *Physical Review D* **104**, 032010 (2021).
- [48] M. Pyle, B. Serfass, P. Brink, B. Cabrera, M. Cherry, N. Mirabol-fathi, L. Novak, B. Sadoulet, D. Seitz, K. Sundqvist, *et al.*, in *AIP Conference Proceedings*, Vol. 1185 (American Institute of Physics, 2009) pp. 223–226.
- [49] L. Cardani, N. Casali, I. Colantoni, A. Cruciani, S. Di Domizio, M. Martinez, V. Pettinacci, G. Pettinari, and M. Vignati, *The European Physical Journal C* **81**, 636 (2021).
- [50] A. Cruciani, L. Bandiera, M. Calvo, N. Casali, I. Colantoni, G. Del Castello, M. del Gallo Roccagiovine, D. Delicato, M. Giammei, V. Guidi, *et al.*, *Applied Physics Letters* **121** (2022).
- [51] S. W. Lemans, *Review of Scientific Instruments* **83** (2012).
- [52] R. Barends, J. Baselmans, S. Yates, J. Gao, J. Hovenier, and T. Klapwijk, *Physical review letters* **100**, 257002 (2008).
- [53] P. J. de Visser, J. Baselmans, J. Bueno, N. Llombart, and T. Klapwijk, *Nature communications* **5**, 3130 (2014).
- [54] J. Zmuidzinas, *Annu. Rev. Condens. Matter Phys.* **3**, 169 (2012).
- [55] J. Baselmans and S. Yates, in *AIP Conference Proceedings*, Vol. 1185 (American Institute of Physics, 2009) pp. 160–163.
- [56] O.-P. Saira, A. Kemppinen, V. F. Maisi, and J. P. Pekola, *Physical Review B* **85**, 012504 (2012).
- [57] D. Ristè, C. Bultink, M. J. Tiggelman, R. N. Schouten, K. W. Lehnert, and L. DiCarlo, *Nature communications* **4**, 1913 (2013).
- [58] Y.-Y. Chang, *SuperCDMS HVeV Run 2 Low-Mass Dark Matter Search, Highly Multiplexed Phonon-Mediated Particle Detector with Kinetic Inductance Detector, and the Blackbody Radiation in Cryogenic Experiments* (California Institute of Technology, 2023).
- [59] R. A. Moffatt, *Two-dimensional spatial imaging of charge transport in germanium crystals at cryogenic temperatures* (Stanford University, 2016).
- [60] J. M. Martinis and K. Osborne, arXiv preprint cond-mat/0402415 (2004).
- [61] K. Serniak, S. Diamond, M. Hays, V. Fatemi, S. Shankar, L. Frunzio, R. Schoelkopf, and M. Devoret, *Physical Review Applied* **12**, 014052 (2019).
- [62] R. Lutchyn, L. Glazman, and A. Larkin, *Physical Review B* **72**, 014517 (2005).
- [63] R. Lutchyn and L. Glazman, *Physical Review B* **75**, 184520 (2007).
- [64] D. Averin and K. Likharev, *Journal of low temperature physics* **62**, 345 (1986).
- [65] K. R. Amin, A. M. Eriksson, M. Kervinen, L. Andersson, R. Rehammar, and S. Gasparinetti, arXiv preprint arXiv:2404.01277 (2024).
- [66] V. Manucharyan, *Superinductance* (2012).
- [67] P. Echternach, K. Stone, C. Bradford, P. Day, D. Wilson, K. Megerian, N. Llombart, and J. Bueno, *Applied Physics Letters* **103** (2013).
- [68] N. Zobrist, G. Coiffard, B. Bumble, N. Swimmer, S. Steiger, M. Daal, G. Collura, A. B. Walter, C. Bockstiegel, N. Fruitwala, *et al.*, *Applied Physics Letters* **115** (2019).
- [69] P. De Visser, J. Baselmans, P. Diener, S. Yates, A. Endo, and T. Klapwijk, *Journal of Low Temperature Physics* **167**, 335 (2012).
- [70] U. Fano, *Physical Review* **72**, 26 (1947).
- [71] P. Verhoeve, N. Rando, A. Peacock, A. Van Dordrecht, A. Poelaert, and D. Goldie, *IEEE transactions on applied superconductivity* **7**, 3359 (1997).
- [72] L. V. Abdurakhimov, I. Mahboob, H. Toida, K. Kakuyanagi, Y. Matsuzaki, and S. Saito, *PRX Quantum* **3**, 040332 (2022).
- [73] O. Noroozian, J. Gao, J. Zmuidzinas, H. G. LeDuc, and B. A. Mazin, in *AIP Conference Proceedings*, Vol. 1185 (American Institute of Physics, 2009) pp. 148–151.
- [74] J. J.-C. Yen, *Phonon Sensor Dynamics For Cryogenic Dark Matter Search Experiment: A Study Of Quasiparticle Transport In Aluminum Coupled To Tungsten Transition Edge Sensors* (Stanford University, 2015).
- [75] J. Yen, J. Kreikebaum, B. A. Young, B. Cabrera, R. Moffatt, P. Redl, B. Shank, P. Brink, M. Cherry, and A. Tomada, *Journal of Low Temperature Physics* **184**, 30 (2016).
- [76] B. A. Mazin, in *Handbook of Superconductivity* (CRC Press, 2022) pp. 756–765.
- [77] S. Hsieh and J. L. Levine, *Physical Review Letters* **20** (1968).
- [78] Y. Dong, Y. Li, W. Zheng, Y. Zhang, Z. Ma, X. Tan, and Y. Yu, *Applied Sciences* **12**, 8461 (2022).
- [79] N. Kurinsky, *The low-mass limit: Dark matter detectors with eV-scale energy resolution* (Stanford University, 2018).
- [80] C. Wang, Y. Y. Gao, I. M. Pop, U. Vool, C. Axline, T. Brecht, R. W. Heeres, L. Frunzio, M. H. Devoret, G. Catelani, L. I. Glazman, and R. J. Schoelkopf, *Nature Communications* **5**, 5836 (2014), arXiv:1406.7300 [cond-mat, physics:quant-ph].
- [81] M. Masuzawa, K. Tsuchiya, A. Terashima, A. Dael, O. Napoloy, and J. Plouin, *SRF2013*, Paris, France (2013).
- [82] M. H. Kelsey, R. Agnese, Y. F. Alam, I. A. Langroudy, E. Azadbakht, D. Brandt, R. Bunker, B. Cabrera, Y.-Y. Chang, H. Coombes, *et al.*, *Nuclear Instruments and Methods in Physics*

Research Section A: Accelerators, Spectrometers, Detectors and Associated Equipment **1055**, 168473 (2023).

- [83] M. Martinez, L. Cardani, N. Casali, A. Cruciani, G. Pettinari, and M. Vignati, *Physical Review Applied* **11**, 064025 (2019).
- [84] M. McEwen, L. Faoro, K. Arya, A. Dunsworth, T. Huang, S. Kim, B. Burkett, A. Fowler, F. Arute, J. C. Bardin, *et al.*, *Nature Physics* **18**, 107 (2022).
- [85] D. Rosenberg, D. Kim, R. Das, D. Yost, S. Gustavsson, D. Hover, P. Krantz, A. Melville, L. Racz, G. Samach, *et al.*, *npj quantum information* **3**, 42 (2017).
- [86] J. Goupy, J. Colas, M. Calvo, J. Billard, P. Camus, R. Germond, A. Juillard, L. Vagneron, M. De Jesus, F. Levy-Bertrand, *et al.*, *Applied Physics Letters* **115** (2019).
- [87] P. De Visser, J. Baselmans, S. Yates, P. Diener, A. Endo, and T. Klapwijk, *Applied Physics Letters* **100** (2012).
- [88] G. Angloher, S. Banik, G. Benato, A. Bento, A. Bertolini, R. Breier, C. Bucci, J. Burkhart, L. Canonica, A. D'Addabbo, *et al.*, *Physical Review D* **107**, 122003 (2023).
- [89] J. Collar, *Physical Review D* **98**, 023005 (2018).
- [90] B. Palmer, C. Sanchez, A. Naik, M. Manheimer, J. Schneiderman, P. Echternach, and F. Wellstood, *Physical Review B* **76**, 054501 (2007).
- [91] C. Owen and D. Scalapino, *Physical Review Letters* **28**, 1559 (1972).
- [92] J. M. Martinis, M. Ansmann, and J. Aumentado, *Physical Review Letters* **103**, 097002 (2009).
- [93] S. Friedrich, K. Segall, M. Gaidis, C. Wilson, D. Prober, A. Szymkowiak, and S. Moseley, *Applied physics letters* **71**, 3901 (1997).
- [94] J. M. Gordon and A. Goldman, *Physical Review B* **34**, 1500 (1986).

Appendix A: Pulse Dynamics

Ref. [58] outlines a quasiparticle pulse model inclusive of a generation-recombination [69] mechanism to explain the quiescent quasiparticle population. We take a simpler tack and work in the limit that the quiescent density $n_0 \ll N_{\text{qp}}^r/V$ so that $n_{\text{qp}}(t) = \delta n_{\text{qp}}(t)$. The quasiparticle conservation equation, assuming a fixed quasiparticle recombination time, reads,

$$\frac{dn_{\text{qp}}}{dt} = \eta_{\text{ph}} \frac{P(t)}{V\Delta} - \frac{n_{\text{qp}}}{\tau_{\text{qp}}}, \quad (\text{A1})$$

where $P(t)$ is the phonon pulse power from the substrate and the second term reflects the recombination process. As we have argued, if both the quasiparticle and phonon rise times in the system are fast, then $P(t)$ can be modeled as a simple exponential described by the phonon decay time:

$$\frac{dn_{\text{qp}}}{dt} = \frac{E_{\text{dep}}}{\tau_{\text{abs}}} e^{-t/\tau_{\text{abs}}}. \quad (\text{A2})$$

We have also assumed that there is only one absorptive surface, otherwise $P(t)$ should reflect the energy split of E_{dep} between multiple sensors. Eq. A1 can be solved analytically via Fourier transform to yield our desired expression of Eq. 3.

Appendix B: Tunneling Rate

We first reproduce a derivation for the chemical potential shift (as found in Ref. [12]) that sources the diffusion pressure for the quasiparticle tunneling. Following Ref. [90] closely in this section, we start by noting that the total quasiparticle density in a volume will be a sum of the non-equilibrium and residual populations and can be given by,

$$n_{\text{qp}} + n_0 = 2 \int_{\Delta}^{\infty} D_f \frac{\epsilon^2}{\sqrt{\epsilon^2 - \Delta^2}} f_{\text{ne}}(\epsilon) d\epsilon, \quad (\text{B1})$$

where $D_f = 3\eta/2\epsilon_F$ is the normal metal density of states (η is the conduction band electron density, and ϵ_F is the Fermi energy). The fractional term is the BCS density of states term for a superconductor. The factor of 2 accounts for hole-like and electron-like states. If there are only a small number of quasiparticles and the volume is in thermodynamic equilibrium, then the quasiparticle distribution is nominally given by the Fermi function,

$$f(\epsilon) = \frac{1}{1 + e^{\epsilon/k_B T}} \quad (\text{B2})$$

$$\epsilon = \sqrt{\left(\frac{\hbar^2 k^2}{2m} - \mu\right)^2 + \Delta^2},$$

with ϵ denoting the energy of a quasiparticle excitation with wave vector k in a superconducting volume. However, while the non-equilibrium quasiparticle population likely thermalizes rapidly ($\ll \mu s$) to equilibrium temperature T , it is *not* in chemical equilibrium. Thus, the chemical potential is shifted

by $\delta\mu$ and the non-equilibrium quasiparticle distribution can instead be modeled by the Owen-Scalapino [91] form,

$$f_{\text{ne}}(\epsilon) = \frac{1}{1 + e^{(\epsilon - \delta\mu)/k_B T}}. \quad (\text{B3})$$

Ref. [90] solves for the expression of the chemical potential shift in terms of the non-equilibrium quasiparticle density by re-expressing Eq. B1 through,

$$n_{\text{qp}} = 2D_f \int_{\Delta}^{\infty} \frac{\epsilon^2}{\sqrt{\epsilon^2 - \Delta^2}} (f_{\text{ne}}(\epsilon) - f(\epsilon)) d\epsilon, \quad (\text{B4})$$

which to lowest order in $k_B T/\Delta$ results in,

$$\delta\mu \approx k_B T \ln \left[1 + \frac{n_{\text{qp}}}{\mathcal{N}} e^{\Delta/k_B T} \right], \quad (\text{B5})$$

where $\mathcal{N} = D_f \sqrt{2\pi\Delta k_B T}$ is the density of available quasiparticle states. At low temperatures such that $n_{\text{qp}} e^{\Delta/k_B T} \gg \mathcal{N}$, per Ref. [12], the above expression reduces to,

$$\delta\mu \approx \Delta + k_B T \ln \left[\frac{n_{\text{qp}}}{\mathcal{N}} \right]. \quad (\text{B6})$$

In the case of asymmetric absorber and island, the terms in Eq. B6 are indexed by their respective locations. Otherwise equal for both pads.

We base our calculation of tunneling rates on Refs. [61, 92] and particularly [13, 14]. The quasiparticle tunneling Hamiltonian is,

$$H_T = \tilde{t} \sum_{l,r,s} \left[(u_r u_l - v_r v_l) \cos \frac{\hat{\phi}}{2} + i(u_r u_l + v_r v_l) \sin \frac{\hat{\phi}}{2} \right] \gamma_{r,s}^\dagger \gamma_{l,s} + \text{H.C.}, \quad (\text{B7})$$

where \tilde{t} is a tunneling matrix element, $\hat{\phi}$ is the phase operator, (u, v) are electron and hole occupation factors indexed by the left (l) and right (r) electrode of the tunnel junction, and γ are fermionic annihilation/creation operators (s indexing spin). The tunneling (parity transition) rate from state i to j can be computed using Fermi's Golden Rule:

$$\Gamma_{ij} = \frac{1}{\hbar} \sum_{l,r,s} |\langle j, r | H_T | i, l \rangle|^2 \delta_{\delta\epsilon_{ij} + \epsilon_l - \epsilon_r}, \quad (\text{B8})$$

where the delta function enforces energy conservation ($\delta\epsilon_{ij}$ is the energy difference between states and $\epsilon_{l,r}$ is energy level of each electrode). Ref. [14] shows that insertion of Eq. B7 in Eq. B8 yields,

$$\Gamma_{ij} = \frac{16E_J}{\pi\hbar} \left(|\langle j | \cos \frac{\hat{\phi}}{2} | i \rangle|^2 S_{ij}^- + |\langle j | \sin \frac{\hat{\phi}}{2} | i \rangle|^2 S_{ij}^+ \right), \quad (\text{B9})$$

where in the low-energy regime the tunneling rate has been factorized into two components: the matrix elements account for qubit dynamics while the S_{ij}^\pm are spectral functions that determine the kinetics of quasiparticle tunneling. In this detector concept, we do not rely on state changes and hence primarily work only with the ground state ($i = 0, j = 0, \delta\epsilon_{ij} \sim 0$). Further, the electrodes are equivalent ($\epsilon_{l,r} \rightarrow \epsilon$) with equivalent

chemical potential shifts. The only relevant spectral function is, after simplifying and substituting coherence factors,

$$S_{00}^{\pm} = \frac{1}{\Delta} \int_{\Delta}^{\infty} d\epsilon f_{ne}(\epsilon) [1 - f_{ne}(\epsilon)] \frac{\epsilon^2}{\epsilon^2 - \Delta^2} \left(1 \pm \frac{\Delta^2}{\epsilon^2} \right). \quad (\text{B10})$$

For the transmon case, where $\chi = E_C/E_J \ll 1$, the cos and sin terms are shown in [13] to reduce to,

$$\begin{aligned} |\langle 0, p | \cos \frac{\hat{\phi}}{2} | 0, p \rangle| &\approx 1 - \frac{1}{2} \sqrt{\frac{E_C}{8E_J}} - \frac{3}{64} \frac{E_C}{E_J} \sim 0.9 \approx 1 \\ |\langle 0, p | \sin \frac{\hat{\phi}}{2} | 0, p \rangle| &\approx |\sin(2\pi n_g)| \left(\frac{2}{3} \right)^{2/3} \\ &\times \Gamma \left(\frac{1}{3} \right) \left(\frac{E_C}{8E_J} \right)^{1/6} \frac{\epsilon_i}{\omega_p} \approx 0, \end{aligned} \quad (\text{B11})$$

where Γ in the last expression is the gamma function.

Inserting Eqs. B10 and B11 into B9 with the help of B6, we obtain:

$$\begin{aligned} \Gamma_{00} &= \frac{32E_J}{h} \frac{1}{\Delta} \int_{\Delta}^{\infty} f_{ne}(1 - f_{ne}) d\epsilon \\ &= \frac{16E_J}{h\Delta} \int_{\Delta}^{\infty} \frac{1}{1 + \cosh(\frac{\epsilon - \delta\mu}{k_B T})} d\epsilon \\ &= \frac{16E_J k_B T}{h\Delta} \frac{1}{1 + e^{(\Delta - \delta\mu)/k_B T}} \\ &\approx \frac{16E_J k_B T}{h\Delta} \frac{1}{1 + \frac{N}{n_{\text{qp}}}} \approx \boxed{\frac{16E_J k_B T}{N\Delta h} n_{\text{qp}} \equiv K n_{\text{qp}}}, \end{aligned} \quad (\text{B12})$$

where we have assumed $n_{\text{qp}} \ll N$ in arriving at the final expression. Eq. 8 is thus proven.

Appendix C: Diffusion & Tunneling Simulations within the Leads

We have made the assumption that n_{qp} thermalizes rapidly and is uniform throughout the absorber, motivating the use of a chemical shift. In reality, quasiparticle deposits in the absorber take time to diffuse to the junction and tunnel across. We briefly investigated the validity of this prescription, following Ref. [80], by modeling quasiparticle diffusion and tunneling as,

$$\begin{aligned} \frac{\partial u(x, y, t)}{\partial t} &= D \nabla^2 u(x, y, t) - \frac{K}{V_j} u(x, y, t) \delta(\vec{r} - \vec{r}_j) \\ &\quad - \frac{1}{\tau_{\text{qp}}} u(x, y, t). \end{aligned} \quad (\text{C1})$$

We assume reflective Neumann boundary conditions and have reduced the problem to two-dimensions (as film thickness \ll phonon absorber size). Tunneling is modeled as a delta-function sink term. We model the quasiparticle lifetime τ_{qp} via recombination but impose an upper limit $\tau_{\text{qp}, \text{max}} = 1$ ms [54]. We use a value of $K \approx 3$ kHz μm^3 similar to Sec. IV B. V_j is the volume of the junction, r_j is the location of the

junction. $u(x, y, t)$ is normalized to unity such that it can be interpreted as the PDF of a quasiparticle in the absorber. We set $D = 22.5$ cm² s⁻¹ as the quasiparticle diffusion constant, measured in Ref. [77]. The value of the diffusion constant and the effective maximum diffusion distance in aluminum are debated quantities, with certain reports indicating poor diffusion for thin (< 100 nm) films [42, 74, 75]. Refs. [78, 92, 93] provide a prescription,

$$\begin{aligned} D &= 60 \text{ cm}^2 \text{ s}^{-1} \cdot v_{\text{qp}} \\ v_{\text{qp}} &= \left(1 - \frac{\Delta^2}{E_{\text{qp}}^2} \right)^{1/2}, \end{aligned} \quad (\text{C2})$$

where v_{qp} is the normalized quasiparticle velocity for a quasiparticle energy E_{qp} . This model is consistent with a measured $D \approx 34$ cm² s⁻¹ in 20 nm thick aluminium (thinner than our proposed absorbers), performed by a subset of authors of this paper. They extracted the diffusion constant through its relationship to the critical superconducting field H_c as per Ref. [94]. Eq. C2 suggests that, at an operating temperature of $O(100)$ mK, with $E_{\text{qp}} = \Delta + k_B T$, a diffusion constant of $D \approx 20$ cm² s⁻¹ is reasonable. Furthermore, the diffusion distance is $\sqrt{2D\tau_{\text{qp}}} \approx O(\text{mm})$ using these parameters, which is significantly larger than any linear dimension of even the largest considered absorbers.

The instant diffusion limit ($D \rightarrow \infty$) solution of Eq. C1 is equivalent to having the junction be the entire volume of the absorber: $\dot{u}(t) = -Ku(t)/V - u(t)/\tau_{\text{qp}}$. The normalized absorber quasiparticle density thus becomes $u(t) = e^{-t/\tau_t} e^{-t/\tau_{\text{qp}}}$, where $\tau_t = V/K$ is the tunneling time. We compare this regime to one with the measured diffusion constant, and simulate solutions to Eqn (C1) using standard finite-difference techniques. From this process, we ascertain a few things: 1) agreement between the simulated solution and the instant diffusion limit justify our use of a uniform quasiparticle density, n_{qp} , and a chemical potential, $\delta\mu$, across the absorber; 2) quasiparticles become uniformly distributed over the absorber regardless of the initial location of the energy deposition; 3) $\tau_{\text{qp}} \ll \tau_t$ so recombination dominates over tunneling. In particular, we can view the tunneling rate as an appropriate measure of the absorber quasiparticle density; 4) Eq. 3 is a good description of this recombination-dominated quasiparticle density. In totality, the results obtained from the simulation are consistent with the conclusions presented in Sec. III.

Appendix D: Absorber and Trap Balance

A simplified model of the steady-state quasiparticle population within the trap and absorber can be written as set of coupled differential equations. The density in the absorber can be expressed as,

$$\frac{dn_{\text{qp,abs}}}{dt} = \frac{1}{V_{\text{abs}}} (\Gamma_{\text{gen}}^{\text{abs}} - \Gamma_{\text{rec}}^{\text{abs}}) - \frac{V_{\text{tr}}}{V_{\text{abs}}} \frac{n_{\text{qp,abs}}}{\tau_{\text{tr}}}, \quad (\text{D1})$$

where $\Gamma_{\text{gen,rec}}^{\text{abs}}$ are quasiparticle generation and recombination (GR) terms, inclusive of any thermal or pair-breaking radiation

contribution. The last term represents the fractional loss into the trap with an assumed trapping timescale τ_{tr} related to the phonon emission timescale (among other considerations). We have assumed perfect transmission across the absorber-trap interface to better highlight the effect of trapping on densities. The corresponding equation for the trap is,

$$\frac{dn_{\text{qp,tr}}}{dt} = \frac{1}{V_{\text{tr}}}(\Gamma_{\text{gen}}^{\text{tr}} - \Gamma_{\text{rec}}^{\text{tr}}) + \frac{n_{\text{qp,abs}}}{\tau_{\text{tr}}}\eta_{\text{pb}}\frac{\Delta_{\text{abs}}}{\Delta_{\text{tr}}}, \quad (\text{D2})$$

where the first term corresponds again to quasiparticle generation and recombination and the second term is the source term

due to trapping. While experimental input will be required to correctly constrain such a model, we can use reasonable assumptions to evaluate the dynamics. We assume thermal densities in line with a 0.025 K operating temperature, a $O(1)$ ms quasiparticle lifetime in the absorber, a $O(100)$ μs lifetime within the trap, a $O(10)$ μs trapping timescale, and a constant injection of quasiparticles into the absorber that would at steady-state result in an absorber density of $\sim 0.05 \text{ qp}\cdot\mu\text{m}^{-3}$. Solving the system of equations, we arrive at our conclusion from Sec. IV B: at steady state, the trap quasiparticle density can be greatly elevated from its quiescent value and can be up to an order-of-magnitude larger.